

Preserving general physical properties in model reduction of dynamical systems via constrained-optimization projection

Alexander Schein^{a,*}, Kevin T. Carlberg^{c,b,**}, Matthew J. Zahr^d.

^a*Technical University of Munich*

^b*Sandia National Laboratories*

^c*University of Washington*

^d*University of Notre Dame*

Abstract

Model-reduction techniques aim to reduce the computational complexity of simulating dynamical systems by applying a (Petrov–)Galerkin projection process that enforces the dynamics to evolve in a low-dimensional subspace of the original state space. Frequently, the resulting reduced-order model (ROM) violates intrinsic physical properties of the original full-order model (FOM) (e.g., global conservation, Lagrangian structure, state-variable bounds) because the projection process does not generally ensure preservation of these properties. However, in many applications, ensuring the ROM preserves such intrinsic properties can enable the ROM to retain physical meaning and lead to improved accuracy and stability properties. In this work, we present a general constrained-optimization formulation for projection-based model reduction that can be used as a template to enforce the ROM to satisfy specific properties on the kinematics and dynamics. We introduce constrained-optimization formulations at both the time-continuous (i.e., ODE) level, which leads to a constrained Galerkin projection, and at the time-discrete level, which leads to a least-squares Petrov–Galerkin (LSPG) projection, in the context of linear multistep schemes. We demonstrate the ability of the proposed formulations to equip ROMs with desired properties such as global energy conservation and bounds on the total variation.

Keywords: projection-based model reduction, Galerkin projection, least-squares Petrov–Galerkin projection, constrained optimization

1. Introduction

Serving as a bridge to overcome the prohibitive computational cost of simulating large-scale, parameterized dynamical systems in time-critical scenarios, projection-based model reduction has gained popularity and yielded successes across problems in many applications, including fluid dynamics, structural dynamics, and reacting flows. In the context of proper orthogonal decomposition (POD) [26] or reduced-basis method [25] approaches, a computationally costly *offline stage* is first executed in which the parameterized dynamical system, or *full-order model* (FOM), is simulated at multiple parameter instances. Then, the state snapshots arising from these training simulations are employed to construct a low-dimensional affine trial subspace of the original state space; recent approaches have also investigated constructing low-dimension nonlinear trial manifolds [18] from these snapshots. A parameterized dynamical system of lower dimension, called the reduced-order model (ROM) is computed by performing a (Petrov–)Galerkin projection process of the

*Parkring 35, 85748 Garching b. München

**7011 East Ave, Livermore, CA 94550

Notre Dame, Indiana, USA 46556

Email addresses: schein@mhpc.mw.tum.de (Alexander Schein), ktcarlb@uw.edu (Kevin T. Carlberg), mzahr@nd.edu (Matthew J. Zahr)

original dynamical system onto this subspace; as a result, the ROM’s solution is restricted to evolve in the low-dimensional trial subspace. If the FOM operators are nonlinear in the state or non-affine in the parameters, then an additional ‘hyper-reduction’ approximation is required to ensure the resulting ROM simulation incurs an operation count that is independent of the FOM state-space dimension. Computational-cost savings are achieved in the *online stage* by simulating the low-cost ROM at new parameter instances.

The ROM approximation typically does not preserve important intrinsic properties of the dynamical system, e.g., global conservation and hyperbolicity in the context of (semi-discretized) conservation laws [8] and energy conservation in the context of solid dynamics [3, 12]. Failure of the ROM to preserve these properties not only raises questions about the physical interpretability of the resulting solution, it also has been attributed to large state-space errors and lack of stability [9], which has motivated research on structure-preserving model reduction for different classes of dynamical systems. One class of such approaches derives governing equations for the ROM in a manner that preserves the structure of the original dynamical system, for example by preserving Lagrangian structure [9, 16], the principle of virtual work [12, 13], (Port-)Hamilton structure [24, 1, 23], the principle of mass conservation [19], or positivity of contact forces in adhesion-free normal contact [4]. Researchers have pursued several works on structure-preserving model reduction in computational fluid dynamics. Refs. [29, 2] investigate conservative ROMs for fluid flows based on preservation of operator skew-symmetry. In Ref. [21], the authors enhance a previously introduced strategy for projection-based ROM construction with data-driven correction by physically motivated constraints ensuring energy dissipation by the correction, while Ref. [20] proposes a data-driven regression model with an energy-conservation constraint on the nonlinear operator of the Navier–Stokes equations. Ref. [28] proposes a technique to preserve the stability property of an equilibrium point at the origin by applying a physically interpretable energy-based inner product for construction of a compressible flow projection-based ROM. Ref. [5] constructs a projection-based ROM incorporating a power balance constraint aiming at physical representation of the incompressible flow energy cascade, and Ref. [22] demonstrates energy conservation by a Stokes extension of boundary conditions.

Another strategy that is gaining increasing attention is the incorporation of equality and inequality constraints that explicitly impose desired behavior in the kinematics and dynamics, such as bounds on the coefficients of POD modes [14], bounds on the temperature of a reacting flow [15], boundary-condition constraints [6], conservation constraints for finite-volume models [8, 17], constraints on the gas void fraction for bubbling fluidized beds [27], and constraints on aerodynamic coefficients (lift, drag, moment) for steady flows [32].

To our knowledge, all existing approaches for structure-preserving model reduction focus on enforcing *problem-specific properties* on the ROM solution; there is no general model-reduction formulation that can be applied to enforce a variety of structure-preserving constraints. As such, researchers currently must re-derive a structure-preserving projection scheme for each problem of interest. The goal of this work is to fill this gap by developing a general projection-based model-reduction formulation that can be employed to enforce a variety of general constraints; as such, it may be used as a template to define a particular instance of a structure-preserving ROM. Our approach comprises a novel constrained-optimization-based formulation applicable to dynamical systems expressed as systems of parameterized ordinary differential equations (ODEs). The formulation supports the following:

- *Constrained Galerkin and least-squares Petrov–Galerkin (LSPG) projection.* We propose two different constrained-optimization formulations: one that operates on the (time-continuous) parameterized system of ODEs (i.e., Galerkin projection), and one that operates on the (time-discrete) parameterized system (i.e., least-squares Petrov–Galerkin projection) [7].
- *Equality and inequality constraints.* Given that desired ROM properties might associate with both equality (e.g., conservation of energy) and inequality (e.g., diminishing total variation in time) constraints, the proposed formulation incorporates both of these types of constraints.
- *Constraints on both kinematics and dynamics.* Given that desired ROM properties might involve both *dynamics constraints* that act on both the state and velocity (e.g., vanishing sum of ODE-

residual entries) and *kinematics constraints* that act exclusively on the state (e.g., bounded state total variation), our formulation supports both types of constraints.

Additionally, we employ this formulation to derive four different problem-specific constraints and perform numerical experiments on a number of parameterized dynamical systems that result from the semi-discretization of partial differential equations: 1D Burgers' equation, 1D Euler equations, and the 2D diffusion equation. These numerical experiments demonstrate that the proposed formulation can be used to derive structure-preserving ROMs that can be equipped with the desired properties.

Because the focus of this paper is on developing a novel projection scheme for model reduction, we do not directly consider hyper-reduction in this initial work; the reader is referred to Ref. [8], which derived hyper-reduction approaches for conservative reduced-order models that can be considered a specific instance of the present framework.¹ As such, we employ the general purpose optimization and root finding functionality from the package `SciPy optimize` [30] in the numerical results.

The remainder of this paper is organized as follows. Section 2 formulates the parameterized dynamical system that defines the FOM and introduces the class of linear multistep schemes we consider for temporal discretization. Section 3 recalls traditional Galerkin and LSPG projections and their associated (unconstrained) minimization problems. Section 4 introduces the proposed constrained-optimization formulations at both the time-continuous and time-discrete levels. Section 5 derives specific exemplary constraints using this general framework. Section 6 presents three numerical experiments that employ these constraints. Finally, Section 7 concludes the paper.

2. Full-order model

We begin by introducing the FOM, which corresponds to a parameterized system of ordinary differential equations (ODEs):

$$\dot{\mathbf{x}} = \mathbf{f}(\mathbf{x}, t; \boldsymbol{\mu}), \quad \mathbf{x}(0; \boldsymbol{\mu}) = \mathbf{x}^0(\boldsymbol{\mu}), \quad (1)$$

where $t \in [0, T]$ denotes the time with $T \in \mathbb{R}_+$ denoting the final time, $\boldsymbol{\mu} \in \mathcal{D}$ denotes a vector of parameters that lives in a parameter domain $\mathcal{D} \subset \mathbb{R}^{n_\mu}$, $\mathbf{x} : [0, T] \times \mathcal{D} \rightarrow \mathbb{R}^N$ denotes the time-dependent, parameterized dynamical-system state (i.e., FOM ODE solution) implicitly defined as the solution to equation (1), $\mathbf{x}^0 : \mathcal{D} \rightarrow \mathbb{R}^N$ denotes the initial condition, and $\mathbf{f} : \mathbb{R}^N \times [0, T] \times \mathbb{R}^{n_\mu} \rightarrow \mathbb{R}^N$ denotes the velocity. As expressed in equation (1), we typically drop the arguments $(t; \boldsymbol{\mu})$ from the state $\mathbf{x}(t; \boldsymbol{\mu})$ and its time derivative $\dot{\mathbf{x}}(t; \boldsymbol{\mu})$ for notational convenience. In residual form, we can express equation (1) as

$$\mathbf{r}(\dot{\mathbf{x}}, \mathbf{x}, t; \boldsymbol{\mu}) = \mathbf{0}, \quad (2)$$

where

$$\mathbf{r} : (\mathbf{v}, \boldsymbol{\xi}, \tau; \boldsymbol{\nu}) \mapsto \mathbf{v} - \mathbf{f}(\boldsymbol{\xi}, \tau; \boldsymbol{\nu}) \quad (3)$$

with $\mathbf{r} : \mathbb{R}^N \times \mathbb{R}^N \times [0, T] \times \mathbb{R}^{n_\mu} \rightarrow \mathbb{R}^N$ denoting the time-continuous residual.

Computing a numerical solution to equation (1) requires introducing a time-discretization method. In this work, we consider the class of linear multistep schemes [7]. Application of a linear multistep scheme to (1) yields the time-discrete dynamical system (OΔE) corresponding to a sequence of algebraic equations

$$\mathbf{r}^n(\mathbf{x}^n; \boldsymbol{\mu}) = \mathbf{0}, \quad n = 1, \dots, N_T, \quad (4)$$

where

$$\mathbf{r}^n : (\boldsymbol{\xi}; \boldsymbol{\nu}) \mapsto \alpha_0 \boldsymbol{\xi} - \Delta t \beta_0 \mathbf{f}(\boldsymbol{\xi}, t^n; \boldsymbol{\nu}) + \sum_{j=1}^k \alpha_j \mathbf{x}^{n-j} - \Delta t \sum_{j=1}^k \beta_j \mathbf{f}(\mathbf{x}^{n-j}, t^{n-j}; \boldsymbol{\nu}), \quad n = 1, \dots, N_T \quad (5)$$

¹Unsurprisingly, the key idea is that any nonlinear terms that appear in either the objective function or constraints must be approximated via hyper-reduction in order to realize computational-cost reduction.

with $\mathbf{r}^n : \mathbb{R}^N \times \mathbb{R}^{n_\mu} \rightarrow \mathbb{R}^N$, $n = 1, \dots, N_T$ denoting the time-discrete residual and $\Delta t = T/N_T$ denoting the times step (assumed to be constant for notational simplicity). Selection of the coefficients α_j , $j = 0, \dots, k$ with $\sum_{j=0}^k \alpha_j = 0$ and β_j , $j = 0, \dots, k$ returns a particular linear multistep scheme; the case $\beta_0 = 0$ yields an explicit scheme. Solving equation (4) yields the parameterized time-discrete dynamical-system state (i.e., FOM OΔE solution) $\mathbf{x}^n(\boldsymbol{\mu}) \approx \mathbf{x}((n)\Delta t; \boldsymbol{\mu})$, $n = 1, \dots, N_T$.

3. Unconstrained dimensional reduction

We now review traditional Galerkin and LSPG projection schemes and recall their associated (unconstrained) minimization properties that we will build upon to define the proposed formulation.

3.1. Low-dimensional-subspace approximation

Given a low-dimensional subspace spanned by the columns of the orthogonal reduced-order basis matrix $\Phi \in V_p(\mathbb{R}^N)$, where $V_m(\mathbb{R}^N)$ denotes the set of orthogonal $n \times m$ real-valued matrices (the Stiefel manifold) and $p \ll N$, projection-based ROMs approximate the kinematics of the problem by restricting the state to reside a low-dimensional affine subspace, which leads to the time-continuous ROM state and velocity

$$\tilde{\mathbf{x}}(t, \boldsymbol{\mu}) := \mathbf{x}_{\text{ref}}(\boldsymbol{\mu}) + \Phi \hat{\mathbf{x}}(t, \boldsymbol{\mu}), \quad (6)$$

$$\dot{\tilde{\mathbf{x}}}(t, \boldsymbol{\mu}) = \Phi \dot{\hat{\mathbf{x}}}(t, \boldsymbol{\mu}), \quad (7)$$

respectively, with $\tilde{\mathbf{x}}, \dot{\tilde{\mathbf{x}}} : [0, T] \times \mathbb{R}^{n_\mu} \rightarrow \mathbb{R}^N$; $\mathbf{x}_{\text{ref}} : \boldsymbol{\mu} \rightarrow \mathbb{R}^N$ denoting a reference state; and $\hat{\mathbf{x}} : [0, T] \times \mathbb{R}^{n_\mu} \rightarrow \mathbb{R}^p$ and $\dot{\hat{\mathbf{x}}} : [0, T] \times \mathbb{R}^{n_\mu} \rightarrow \mathbb{R}^p$ denoting the time-continuous generalized coordinates for the state and velocity, respectively. The time-discrete ROM state then satisfies

$$\tilde{\mathbf{x}}^n(\boldsymbol{\mu}) := \mathbf{x}_{\text{ref}}(\boldsymbol{\mu}) + \Phi \hat{\mathbf{x}}^n(\boldsymbol{\mu}), \quad n = 1, \dots, N_T \quad (8)$$

with $\tilde{\mathbf{x}}^n : \mathbb{R}^{n_\mu} \rightarrow \mathbb{R}^N$, $n = 1, \dots, N_T$ and $\hat{\mathbf{x}}^n : \mathbb{R}^{n_\mu} \rightarrow \mathbb{R}^p$, $n = 1, \dots, N_T$ denoting the time-discrete generalized coordinates for the state. One convenient choice for the reference state comprises $\mathbf{x}_{\text{ref}}(\boldsymbol{\mu}) = \mathbf{x}^0(\boldsymbol{\mu})$, which implies that the initial condition can be exactly satisfied by setting $\hat{\mathbf{x}}(0, \boldsymbol{\mu}) = \hat{\mathbf{x}}^0(\boldsymbol{\mu}) = \mathbf{0}$.

3.2. Galerkin projection

Given the kinematic approximation (6)–(8), Galerkin projection derives the dynamics of the ROM by setting the (time-continuous) velocity to be the minimizer of the time-continuous residual (3) over the trial subspace given the current state, time, and parameters, i.e.,

$$\dot{\hat{\mathbf{x}}} \in \arg \min_{\hat{\mathbf{v}} \in \mathbb{R}^p} \|\mathbf{r}(\Phi \hat{\mathbf{v}}, \mathbf{x}_{\text{ref}}(\boldsymbol{\mu}) + \Phi \hat{\mathbf{x}}, t; \boldsymbol{\mu})\|_2. \quad (9)$$

One can show that necessary stationarity conditions for the solution to (9) are equivalent to the familiar low-dimensional Galerkin ODE system

$$\dot{\hat{\mathbf{x}}} = \Phi^T \mathbf{f}(\mathbf{x}_{\text{ref}}(\boldsymbol{\mu}) + \Phi \hat{\mathbf{x}}, t; \boldsymbol{\mu}). \quad (10)$$

Application of a linear multistep scheme to numerically solve equation (10) yields the time-discrete Galerkin OΔE

$$\hat{\mathbf{r}}_G^n(\hat{\mathbf{x}}^n; \boldsymbol{\mu}) = \mathbf{0}, \quad n = 1, \dots, N_T, \quad (11)$$

where

$$\begin{aligned} \hat{\mathbf{r}}_G^n : (\hat{\boldsymbol{\xi}}; \boldsymbol{\nu}) &\mapsto \alpha_0 \hat{\boldsymbol{\xi}} - \Delta t \beta_0 \Phi^T \mathbf{f}(\mathbf{x}_{\text{ref}}(\boldsymbol{\nu}) + \Phi \hat{\boldsymbol{\xi}}, t^n; \boldsymbol{\nu}) \\ &+ \sum_{j=1}^k \alpha_j \hat{\mathbf{x}}^{n-j} - \Delta t \sum_{j=1}^k \beta_j \Phi^T \mathbf{f}(\mathbf{x}_{\text{ref}}(\boldsymbol{\nu}) + \Phi \hat{\mathbf{x}}^{n-j}, t^{n-j}; \boldsymbol{\nu}), \quad n = 1, \dots, N_T \end{aligned} \quad (12)$$

with $\hat{\mathbf{r}}_G^n : \mathbb{R}^p \times \mathbb{R}^{n_\mu} \rightarrow \mathbb{R}^p$, $n = 1, \dots, N_T$ denoting the time-discrete Galerkin residual. Solving equation (11) yields the parameterized time-discrete Galerkin state $\hat{\mathbf{x}}^n(\boldsymbol{\mu})$, $n = 1, \dots, N_T$.

3.3. Least-squares Petrov–Galerkin projection

Given the kinematic approximation (6)–(8), LSPG projection [7] derives the ROM dynamics by posing a time-discrete optimization problem. That is, it computes the time-discrete ROM state as the minimizer of the time-discrete residual (5) such that

$$\hat{\mathbf{x}}^n \in \arg \min_{\hat{\boldsymbol{\xi}} \in \mathbb{R}^p} \left\| \mathbf{r}^n(\mathbf{x}_{\text{ref}}(\boldsymbol{\mu}) + \boldsymbol{\Phi} \hat{\boldsymbol{\xi}}; \boldsymbol{\mu}) \right\|_2, \quad n = 1, \dots, N_T. \quad (13)$$

One can show that necessary stationarity conditions for the solution to (13) correspond to the LSPG OΔE

$$\hat{\mathbf{r}}_L^n(\hat{\mathbf{x}}^n; \boldsymbol{\mu}) = \mathbf{0}, \quad n = 1, \dots, N_T, \quad (14)$$

where

$$\hat{\mathbf{r}}_L^n : (\hat{\boldsymbol{\xi}}; \boldsymbol{\nu}) \mapsto \boldsymbol{\Phi}^T \left[\frac{\partial \mathbf{r}^n}{\partial \boldsymbol{\xi}}(\mathbf{x}_{\text{ref}}(\boldsymbol{\nu}) + \boldsymbol{\Phi} \hat{\boldsymbol{\xi}}; \boldsymbol{\nu}) \right]^T \mathbf{r}^n(\mathbf{x}_{\text{ref}}(\boldsymbol{\nu}) + \boldsymbol{\Phi} \hat{\boldsymbol{\xi}}; \boldsymbol{\nu}), \quad n = 1, \dots, N_T \quad (15)$$

with $\hat{\mathbf{r}}_L^n : \mathbb{R}^p \times \mathbb{R}^{n_\mu} \rightarrow \mathbb{R}^p$, $n = 1, \dots, N_T$ denoting the time-discrete LSPG OΔE residual.

4. Constrained Galerkin and LSPG projection

This section introduces the proposed constrained Galerkin and LSPG projection techniques. We begin by defining general kinematic and dynamic equality and inequality constraints in Section 4.1. Section 4.2 and 4.3 derive the Galerkin and LSPG projection techniques, respectively.

4.1. General constraint formulation

We introduce a general set of constraints

$$\bar{\mathbf{c}}(\mathbf{x}, t; \boldsymbol{\mu}) = \mathbf{0}, \quad \forall t \in [0, T], \quad \forall \boldsymbol{\mu} \in \mathcal{D}, \quad (16)$$

$$\mathbf{c}(\dot{\mathbf{x}}, \mathbf{x}, t; \boldsymbol{\mu}) = \mathbf{0}, \quad \forall t \in [0, T], \quad \forall \boldsymbol{\mu} \in \mathcal{D}, \quad (17)$$

$$\bar{\mathbf{d}}(\mathbf{x}, t; \boldsymbol{\mu}) \geq \mathbf{0}, \quad \forall t \in [0, T], \quad \forall \boldsymbol{\mu} \in \mathcal{D}, \quad (18)$$

$$\mathbf{d}(\dot{\mathbf{x}}, \mathbf{x}, t; \boldsymbol{\mu}) \geq \mathbf{0}, \quad \forall t \in [0, T], \quad \forall \boldsymbol{\mu} \in \mathcal{D}, \quad (19)$$

where $\geq \mathbf{0}$ denotes componentwise inequality. Equations (16)–(19) can be categorized as either equality or inequality constraints and as either kinematic constraints on the state or dynamic constraints on the velocity (given the state), i.e.,

- kinematic equality constraints

$$\begin{aligned} \bar{\mathbf{c}} : (\boldsymbol{\xi}, \tau; \boldsymbol{\nu}) &\mapsto \bar{\mathbf{c}}(\boldsymbol{\xi}, \tau; \boldsymbol{\nu}) \\ &: \mathbb{R}^N \times [0, T] \times \mathbb{R}^{n_\mu} \rightarrow \mathbb{R}^{n_{\bar{\mathbf{c}}}}, \end{aligned} \quad (20)$$

- dynamic equality constraints

$$\begin{aligned} \mathbf{c} : (\mathbf{v}, \boldsymbol{\xi}, \tau; \boldsymbol{\nu}) &\mapsto \mathbf{c}(\mathbf{v}, \boldsymbol{\xi}, \tau; \boldsymbol{\nu}) \\ &: \mathbb{R}^N \times \mathbb{R}^N \times [0, T] \times \mathbb{R}^{n_\mu} \rightarrow \mathbb{R}^{n_{\mathbf{c}}}, \end{aligned} \quad (21)$$

- kinematic inequality constraints

$$\begin{aligned} \bar{\mathbf{d}} : (\boldsymbol{\xi}, \tau; \boldsymbol{\nu}) &\mapsto \bar{\mathbf{d}}(\boldsymbol{\xi}, \tau; \boldsymbol{\nu}) \\ &: \mathbb{R}^N \times [0, T] \times \mathbb{R}^{n_\mu} \rightarrow \mathbb{R}^{n_{\bar{\mathbf{d}}}}, \end{aligned} \quad (22)$$

- dynamic inequality constraints

$$\begin{aligned} \mathbf{d} : (\mathbf{v}, \boldsymbol{\xi}, \tau; \boldsymbol{\nu}) &\mapsto \mathbf{d}(\mathbf{v}, \boldsymbol{\xi}, \tau; \boldsymbol{\nu}) \\ &: \mathbb{R}^N \times \mathbb{R}^N \times [0, T] \times \mathbb{R}^{n_\mu} \rightarrow \mathbb{R}^{n_d}. \end{aligned} \quad (23)$$

Specific instances representable by our general constraint set can be found in literature. Table D.2 states examples of such constraints.

Remark 4.1. *The purpose of this work is to augment standard minimum-residual reduced-order models with general kinematic and dynamic constraints to enforce structure preservation or other desired properties. However, it is possible to add constraints that render the optimization problem infeasible, which can happen if the optimization problem becomes overconstrained or the reduced basis precludes feasibility, i.e., there is no solution in the reduced subspace that satisfies the constraints. Both of these issues are problem-dependent and are beyond the scope of this work.*

4.2. Constrained Galerkin projection

As can be seen from equation (9), Galerkin projection corresponds to solving a time-continuous optimization problem for the velocity generalized coordinates. As such, we must linearize the kinematic constraints such that they are enforced to first order by the computed velocity. The associated linearizations of constraints (16) and (18) are

$$\frac{\partial \bar{\mathbf{c}}}{\partial \boldsymbol{\xi}}(\mathbf{x}, t; \boldsymbol{\mu}) \dot{\mathbf{x}} + \frac{\partial \bar{\mathbf{c}}}{\partial \tau}(\mathbf{x}, t; \boldsymbol{\mu}) = \mathbf{0}, \quad \forall t \in [0, T], \forall \boldsymbol{\mu} \in \mathcal{D}, \quad (24)$$

$$\frac{\partial \bar{\mathbf{d}}}{\partial \boldsymbol{\xi}}(\mathbf{x}, t; \boldsymbol{\mu}) \dot{\mathbf{x}} + \frac{\partial \bar{\mathbf{d}}}{\partial \tau}(\mathbf{x}, t; \boldsymbol{\mu}) \geq \mathbf{0} \quad \text{if } \bar{\mathbf{d}}(\mathbf{x}, t; \boldsymbol{\mu}) = \mathbf{0}, \quad \forall t \in [0, T], \forall \boldsymbol{\mu} \in \mathcal{D}, \quad (25)$$

respectively. Note that the condition on inequality (25) arises from the need to enforce the constraint to first order only if the constraint is active.

Recalling the definitions of the ROM state (6) and velocity (7), we introduce the set of general Galerkin projection constraints

$$\bar{\mathbf{c}}_G : (\hat{\mathbf{v}}, \hat{\boldsymbol{\xi}}, \tau; \boldsymbol{\nu}) \mapsto \frac{\partial \bar{\mathbf{c}}}{\partial \boldsymbol{\xi}}(\mathbf{x}_{\text{ref}}(\boldsymbol{\nu}) + \boldsymbol{\Phi} \hat{\boldsymbol{\xi}}, \tau; \boldsymbol{\nu}) \boldsymbol{\Phi} \hat{\mathbf{v}} + \frac{\partial \bar{\mathbf{c}}}{\partial \tau}(\mathbf{x}_{\text{ref}}(\boldsymbol{\nu}) + \boldsymbol{\Phi} \hat{\boldsymbol{\xi}}, \tau; \boldsymbol{\nu}), \quad (26)$$

$$\mathbf{c}_G : (\hat{\mathbf{v}}, \hat{\boldsymbol{\xi}}, \tau; \boldsymbol{\nu}) \mapsto \mathbf{c}(\boldsymbol{\Phi} \hat{\mathbf{v}}, \mathbf{x}_{\text{ref}}(\boldsymbol{\nu}) + \boldsymbol{\Phi} \hat{\boldsymbol{\xi}}, \tau; \boldsymbol{\nu}), \quad (27)$$

$$\bar{\mathbf{d}}_G : (\hat{\mathbf{v}}, \hat{\boldsymbol{\xi}}, \tau; \boldsymbol{\nu}) \mapsto \frac{\partial \bar{\mathbf{d}}}{\partial \boldsymbol{\xi}}(\mathbf{x}_{\text{ref}}(\boldsymbol{\nu}) + \boldsymbol{\Phi} \hat{\boldsymbol{\xi}}, \tau; \boldsymbol{\nu}) \boldsymbol{\Phi} \hat{\mathbf{v}} + \frac{\partial \bar{\mathbf{d}}}{\partial \tau}(\mathbf{x}_{\text{ref}}(\boldsymbol{\nu}) + \boldsymbol{\Phi} \hat{\boldsymbol{\xi}}, \tau; \boldsymbol{\nu}), \quad (28)$$

$$\mathbf{d}_G : (\hat{\mathbf{v}}, \hat{\boldsymbol{\xi}}, \tau; \boldsymbol{\nu}) \mapsto \mathbf{d}(\boldsymbol{\Phi} \hat{\mathbf{v}}, \mathbf{x}_{\text{ref}}(\boldsymbol{\nu}) + \boldsymbol{\Phi} \hat{\boldsymbol{\xi}}, \tau; \boldsymbol{\nu}), \quad (29)$$

with $\bar{\mathbf{c}}_G, \mathbf{c}_G, \bar{\mathbf{d}}_G, \mathbf{d}_G : \mathbb{R}^p \times \mathbb{R}^p \times [0, T] \times \mathbb{R}^{n_\mu} \rightarrow \mathbb{R}^\gamma$, $\gamma \in \{n_{\bar{\mathbf{c}}}, n_{\mathbf{c}}, n_{\bar{\mathbf{d}}}, n_{\mathbf{d}}\}$ all velocity dependent.

As a result, the time-continuous constrained Galerkin ODE system is

$$\dot{\hat{\mathbf{x}}} = \hat{\mathbf{f}}(\hat{\mathbf{x}}, t; \boldsymbol{\mu}) \quad (30)$$

with the velocity $\hat{\mathbf{f}} : (\hat{\boldsymbol{\xi}}, \tau; \boldsymbol{\nu}) \mapsto \hat{\mathbf{f}}(\hat{\boldsymbol{\xi}}, \tau; \boldsymbol{\nu})$, $\hat{\mathbf{f}} : \mathbb{R}^p \times [0, T] \times \mathbb{R}^{n_\mu} \rightarrow \mathbb{R}^p$ corresponding to the solution of the optimization problem

$$\begin{aligned} &\underset{\hat{\mathbf{v}} \in \mathbb{R}^p}{\text{minimize}} \quad \left\| \mathbf{r}(\boldsymbol{\Phi} \hat{\mathbf{v}}, \mathbf{x}_{\text{ref}}(\boldsymbol{\nu}) + \boldsymbol{\Phi} \hat{\boldsymbol{\xi}}, \tau; \boldsymbol{\nu}) \right\|_2 \\ &\text{subject to} \quad \bar{\mathbf{c}}_G(\hat{\mathbf{v}}, \hat{\boldsymbol{\xi}}, \tau; \boldsymbol{\nu}) = \mathbf{0} \\ &\quad \quad \quad \mathbf{c}_G(\hat{\mathbf{v}}, \hat{\boldsymbol{\xi}}, \tau; \boldsymbol{\nu}) = \mathbf{0} \\ &\quad \quad \quad \bar{\mathbf{d}}_G(\hat{\mathbf{v}}, \hat{\boldsymbol{\xi}}, \tau; \boldsymbol{\nu}) \geq \mathbf{0} \quad \text{if } \bar{\mathbf{d}}(\mathbf{x}_{\text{ref}}(\boldsymbol{\nu}) + \boldsymbol{\Phi} \hat{\boldsymbol{\xi}}, \tau; \boldsymbol{\nu}) = \mathbf{0} \\ &\quad \quad \quad \mathbf{d}_G(\hat{\mathbf{v}}, \hat{\boldsymbol{\xi}}, \tau; \boldsymbol{\nu}) \geq \mathbf{0}. \end{aligned} \quad (31)$$

The resulting time-discretized constrained Galerkin OΔE is

$$\mathbf{r}_G^n(\hat{\mathbf{x}}^n; \boldsymbol{\mu}) = \mathbf{0}, \quad n = 1, \dots, N_T, \quad (32)$$

where

$$\mathbf{r}_G^n : (\hat{\boldsymbol{\xi}}; \boldsymbol{\nu}) \mapsto \alpha_0 \hat{\boldsymbol{\xi}} - \Delta t \beta_0 \hat{\mathbf{f}}(\hat{\boldsymbol{\xi}}, t^n; \boldsymbol{\nu}) + \sum_{j=1}^k \alpha_j \hat{\mathbf{x}}^{n-j} - \Delta t \sum_{j=1}^k \beta_j \hat{\mathbf{f}}(\hat{\mathbf{x}}^{n-j}, t^{n-j}; \boldsymbol{\nu}), \quad n = 1, \dots, N_T \quad (33)$$

with $\mathbf{r}_G^n : \mathbb{R}^p \times \mathbb{R}^{n_\mu} \rightarrow \mathbb{R}^p$, $n = 1, \dots, N_T$ denoting the constrained Galerkin OΔE residual.

Remark 4.2. *The conditional statement “if $\bar{\mathbf{d}}(\mathbf{x}_{\text{ref}}(\boldsymbol{\nu}) + \Phi \hat{\boldsymbol{\xi}}, \tau; \boldsymbol{\nu}) = \mathbf{0}$ ” in optimization problem (31) is employed to identify active constraints from the time-continuous perspective. In practice, strict fulfillment of the associated kinematic inequality constraint can only be guaranteed for infinitesimally small time steps. Once time discretization is introduced in (32), finite time steps and limited machine precision imply that strict satisfaction of the kinematic inequality will likely fail in practice. To address this, we trigger activation of the constraint by admitting potential violation; that is, the conditional statement in optimization problem (31) after time discretization reads “if $\bar{\mathbf{d}}(\mathbf{x}_{\text{ref}}(\boldsymbol{\nu}) + \Phi \hat{\boldsymbol{\xi}}, \tau; \boldsymbol{\nu}) \leq \mathbf{0}$ ”. As a consequence, slight constraint violations due to time discretization and finite precision will be accepted by the numerical solution.*

4.3. Constrained least-squares Petrov–Galerkin projection

The LSPG projection ROM (13) corresponds to solving a time-discrete optimization problem for the state generalized coordinates. As such, we must discretize the dynamic constraints to convert them into constraints that depend on the state only. To achieve this, we apply the same underlying time-discretization scheme used to discretize the velocity in the governing ODE. In the case of linear multistep schemes, the discretized dynamic constraints can be derived by substituting the time-continuous velocity with its time-discrete variant

$$\bar{\mathbf{v}}^{n-q} : (\boldsymbol{\xi}; \boldsymbol{\nu}) \mapsto \frac{1}{\Delta t \beta_q} (\alpha_0 \boldsymbol{\xi} + \sum_{j=1}^k \alpha_j \mathbf{x}^{n-j} - \Delta t \sum_{j=1}^k \beta_j \mathbf{f}(\mathbf{x}^{n-j}, t^{n-j}; \boldsymbol{\nu})), \quad n = 1, \dots, N_T \quad (34)$$

with $\bar{\mathbf{v}}^{n-q} : \mathbb{R}^N \times \mathbb{R}^{n_\mu} \rightarrow \mathbb{R}^N$ and $q = 0$ for $\beta_0 \neq 0$ (implicit time integration) and $q = 1$ for $\beta_0 = 0$ (explicit time integration). As a consequence, we can express the set of general LSPG constraints as

$$\bar{\mathbf{c}}_L^n : (\hat{\boldsymbol{\xi}}; \boldsymbol{\nu}) \mapsto \bar{\mathbf{c}}(\mathbf{x}_{\text{ref}}(\boldsymbol{\nu}) + \Phi \hat{\boldsymbol{\xi}}, t^n; \boldsymbol{\nu}), \quad (35)$$

$$\mathbf{c}_L^n : (\hat{\boldsymbol{\xi}}; \boldsymbol{\nu}) \mapsto \mathbf{c}(\bar{\mathbf{v}}^{n-q}(\mathbf{x}_{\text{ref}}(\boldsymbol{\nu}) + \Phi \hat{\boldsymbol{\xi}}; \boldsymbol{\nu}), \mathbf{x}_{\text{ref}}(\boldsymbol{\nu}) + \Phi \hat{\boldsymbol{\xi}}_q^n, t^{n-q}; \boldsymbol{\nu}), \quad (36)$$

$$\bar{\mathbf{d}}_L^n : (\hat{\boldsymbol{\xi}}; \boldsymbol{\nu}) \mapsto \bar{\mathbf{d}}(\mathbf{x}_{\text{ref}}(\boldsymbol{\nu}) + \Phi \hat{\boldsymbol{\xi}}, t^n; \boldsymbol{\nu}), \quad (37)$$

$$\mathbf{d}_L^n : (\hat{\boldsymbol{\xi}}; \boldsymbol{\nu}) \mapsto \mathbf{d}(\bar{\mathbf{v}}^{n-q}(\mathbf{x}_{\text{ref}}(\boldsymbol{\nu}) + \Phi \hat{\boldsymbol{\xi}}; \boldsymbol{\nu}), \mathbf{x}_{\text{ref}}(\boldsymbol{\nu}) + \Phi \hat{\boldsymbol{\xi}}_q^n, t^{n-q}; \boldsymbol{\nu}), \quad (38)$$

with $\bar{\mathbf{c}}_L^n, \mathbf{c}_L^n, \bar{\mathbf{d}}_L^n, \mathbf{d}_L^n : \mathbb{R}^p \times \mathbb{R}^{n_\mu} \rightarrow \mathbb{R}^\gamma$, $\gamma \in \{n_{\bar{c}}, n_c, n_{\bar{d}}, n_d\}$ and $q = 0$ for $\beta_0 \neq 0$ and $q = 1$ for $\beta_0 = 0$. For notational convenience we introduced

$$\hat{\boldsymbol{\xi}}_q^n = \begin{cases} \hat{\boldsymbol{\xi}} & \text{for } q = 0 \\ \hat{\mathbf{x}}^{n-1} & \text{for } q = 1, \end{cases} \quad (39)$$

resolving either to the optimization variable $\hat{\boldsymbol{\xi}}$ or to the fixed generalized-coordinates state of the previous time step $\hat{\mathbf{x}}^{n-1}$.

Then, the time-discrete LSPG ROM solution $\hat{\mathbf{x}}^n$, $n = 1, \dots, N_T$ corresponds to the solution to the optimization problem

$$\begin{aligned}
& \underset{\hat{\boldsymbol{\xi}} \in \mathbb{R}^p}{\text{minimize}} && \left\| \mathbf{r}^n(\mathbf{x}_{\text{ref}}(\boldsymbol{\mu}) + \boldsymbol{\Phi} \hat{\boldsymbol{\xi}}; \boldsymbol{\mu}) \right\|_2 \\
& \text{subject to} && \bar{\mathbf{c}}_L^n(\hat{\boldsymbol{\xi}}; \boldsymbol{\mu}) = \mathbf{0} \\
& && \mathbf{c}_L^n(\hat{\boldsymbol{\xi}}; \boldsymbol{\mu}) = \mathbf{0} \\
& && \bar{\mathbf{d}}_L^n(\hat{\boldsymbol{\xi}}; \boldsymbol{\mu}) \geq \mathbf{0} \\
& && \mathbf{d}_L^n(\hat{\boldsymbol{\xi}}; \boldsymbol{\mu}) \geq \mathbf{0}.
\end{aligned} \tag{40}$$

Remark 4.3. *The introduction of the state-to-velocity mapping into the dynamic constraints (36) and (38) is consistent with the time discretization of the FOM. As such, the time-discrete residual (5) can be written in terms of the time-continuous residual (3) as*

$$\mathbf{r}^n(\mathbf{x}^n; \boldsymbol{\mu}) = \Delta t \beta_q \mathbf{r}(\bar{\mathbf{v}}^{n-q}(\mathbf{x}^n; \boldsymbol{\mu}), \mathbf{x}^{n-q}, t^{n-q}; \boldsymbol{\mu}), \tag{41}$$

with $q = 0$ for $\beta_0 \neq 0$ and $q = 1$ for $\beta_0 = 0$, compare with time discretization of the dynamic constraints (36) and (38).

Remark 4.4. *The unconstrained projections require solving a nonlinear system of size p , where the dominant cost comes from evaluating the reduced residual and Jacobian and solving the (dense) linear system at each nonlinear iteration. In contrast, the constrained projections require solving an optimization problem in p variables and $M = n_{\bar{\mathbf{c}}} + n_{\mathbf{c}} + n_{\bar{\mathbf{d}}} + n_{\mathbf{d}}$ constraints. The dominant cost comes from evaluating the residual and its Jacobian, evaluating the constraints and their Jacobian; the system that must be solved (which is usually dense) depends on the optimization solver used. For example, for penalty and augmented Lagrangian methods, the constrained optimization problem is solved by solving a sequence of unconstrained optimization problems whose objective incorporates the original objective function and constraints. The unconstrained problem is usually solved using quasi-Newton methods, which results in a dense linear system of size p . The cost per iteration of such methods for the constrained projection is similar to a nonlinear iteration for the unconstrained projection (depending on the cost of constraint evaluations); however, the constrained problem usually requires more iterations to converge. On the other hand, sequential quadratic programming and primal-dual interior point methods result in higher-dimensional linear systems, which increases the cost per iteration, but they usually converge more rapidly. In this work, $M \leq 3$ so the increased cost per iteration (relative to the unconstrained projection) is negligible.*

Remark 4.5. *The main step required to incorporate hyper-reduction into the constrained model reduction formulation is acceleration of the discrete residual and Jacobian evaluations, which can be achieved using standard techniques [3, 10, 12]. This is the only step required if the constraints can be evaluated at a cost independent of the FOM dimension N (or reduces as such when the model order reduction ansatz is used, e.g., polynomial in \mathbf{x} and $\dot{\mathbf{x}}$). In the case where the constraint evaluations scale with N (e.g., non-polynomial dependence on \mathbf{x} and $\dot{\mathbf{x}}$), hyper-reduction must be incorporated into the constraint functions; see Ref. [4] in the context of contact mechanics and Ref. [8] in the context of fluid mechanics. A general procedure to hyper-reduce constraint functions will be considered in future work.*

5. Specific constraints

The general formulation of kinematic/dynamic equality/inequality constraints presented in Section 4.1 can be employed as a template for defining problem-specific constraints. In this section we derive such specific constraints, which will be enforced in the numerical examples in Section 6.

5.1. Constraint on the sum of residual entries (dynamic equality)

By definition, the time-continuous FOM solution satisfies constraints

$$\mathbf{C}\mathbf{r}(\dot{\mathbf{x}}, \mathbf{x}, t; \boldsymbol{\mu}) = \mathbf{0} \quad (42)$$

and the time-discrete FOM solution satisfies

$$\mathbf{C}\mathbf{r}^n(\mathbf{x}^n; \boldsymbol{\mu}) = \Delta t \beta_q \mathbf{C}\mathbf{r}(\bar{\mathbf{v}}^{n-q}(\mathbf{x}^n; \boldsymbol{\mu}), \mathbf{x}^{n-q}, t^{n-q}; \boldsymbol{\mu}) = \mathbf{0}, \quad n = 1, \dots, N_T \quad (43)$$

for any matrix $\mathbf{C} \in \mathbb{R}^{n_C \times N}$. This type of dynamic equality constraint can be employed to enforce conservation in the case of FOMs associating with finite-volume discretizations of conservation laws [8]. We also consider this type of constraint matrix, and particularly focus on cases where the matrix is composed exclusively of 0 and 1 entries. In this case, equation (42) and (43) return a vector of sums of selected residual entries, in the following we will refer to this type of constraint as a sum-of-residual-entries (rsum) constraint.

The Galerkin projection constraint corresponding to optimization problem (31) reads

$$\mathbf{c}_{G,\text{rsum}}(\hat{\mathbf{v}}, \hat{\boldsymbol{\xi}}, \tau; \boldsymbol{\nu}) = \mathbf{0} \quad (44)$$

using

$$\mathbf{c}_{G,\text{rsum}} : (\hat{\mathbf{v}}, \hat{\boldsymbol{\xi}}, \tau; \boldsymbol{\nu}) \mapsto \mathbf{C}\mathbf{r}(\Phi\hat{\mathbf{v}}, \mathbf{x}_{\text{ref}}(\boldsymbol{\nu}) + \Phi\hat{\boldsymbol{\xi}}, \tau; \boldsymbol{\nu}) \quad (45)$$

with $\mathbf{c}_{G,\text{rsum}} : \mathbb{R}^p \times \mathbb{R}^p \times [0, T] \times \mathbb{R}^{n_\mu} \rightarrow \mathbb{R}^{n_C}$.

The LSPG projection constraint corresponding to optimization problem (40) reads

$$\mathbf{c}_{L,\text{rsum}}^n(\hat{\boldsymbol{\xi}}; \boldsymbol{\mu}) = \mathbf{0}, \quad n = 1, \dots, N_T \quad (46)$$

using

$$\mathbf{c}_{L,\text{rsum}}^n(\hat{\boldsymbol{\xi}}; \boldsymbol{\nu}) \mapsto \mathbf{C}\mathbf{r}^n(\mathbf{x}_{\text{ref}}(\boldsymbol{\nu}) + \Phi\hat{\boldsymbol{\xi}}; \boldsymbol{\nu}) = \Delta t \beta_q \mathbf{C}\mathbf{r}(\bar{\mathbf{v}}^{n-q}(\mathbf{x}_{\text{ref}}(\boldsymbol{\nu}) + \Phi\hat{\boldsymbol{\xi}}; \boldsymbol{\nu}), \mathbf{x}^{n-q}, t^{n-q}; \boldsymbol{\nu}) \quad (47)$$

with $\mathbf{c}_{L,\text{rsum}}^n : \mathbb{R}^p \times \mathbb{R}^{n_\mu} \rightarrow \mathbb{R}^{n_C}$, $n = 1, \dots, N_T$.

5.2. Constraint on diminishing total variation (dynamic inequality)

Another useful property that holds for scalar conservation laws is diminishing total variation (referred to as tvd-constraint in the following). For the case of a 1D problem, the total variation of the solution—in the case of the state \mathbf{x} corresponding to the value of the solution on a 1D uniformly spaced grid—can be expressed as

$$TV(\mathbf{x}) = \sum_{i=1}^{N-1} |[\mathbf{x}]_{i+1} - [\mathbf{x}]_i|, \quad (48)$$

where $[\mathbf{x}]_i$ denotes the i th component of the vector \mathbf{x} . Non-increasing total variation can be expressed as the dynamic inequality constraint

$$\frac{d}{dt} TV(\mathbf{x}) \leq 0, \quad (49)$$

which is equivalent to

$$-\sum_{i=1}^{N-1} \text{sgn}([\mathbf{x}]_{i+1} - [\mathbf{x}]_i) ([\dot{\mathbf{x}}]_{i+1} - [\dot{\mathbf{x}}]_i) \geq 0, \quad (50)$$

wherein we introduced the sign-function $\text{sgn}(x) = \frac{d}{dx}|x|$ for $x \neq 0$. The Galerkin projection constraint corresponding to optimization problem (31) reads

$$d_{G,\text{tvd}}(\hat{\mathbf{v}}, \hat{\boldsymbol{\xi}}, \bullet; \boldsymbol{\nu}) \geq 0 \quad (51)$$

using

$$d_{G,\text{tvd}} : (\hat{\boldsymbol{v}}, \hat{\boldsymbol{\xi}}, \bullet; \boldsymbol{\nu}) \mapsto - \sum_{i=1}^{N-1} \text{sgn}([\mathbf{x}_{\text{ref}}(\boldsymbol{\nu}) + \boldsymbol{\Phi}\hat{\boldsymbol{\xi}}]_{i+1} - [\mathbf{x}_{\text{ref}}(\boldsymbol{\nu}) + \boldsymbol{\Phi}\hat{\boldsymbol{\xi}}]_i)([\boldsymbol{\Phi}\hat{\boldsymbol{v}}]_{i+1} - [\boldsymbol{\Phi}\hat{\boldsymbol{v}}]_i) \quad (52)$$

with $d_{G,\text{tvd}} : \mathbb{R}^p \times \mathbb{R}^p \times \mathbb{R}^{n_\mu} \rightarrow \mathbb{R}$ and \bullet indicating an unused argument of the template constraint (19).

The LSPG projection constraint corresponding to optimization problem (40) reads

$$d_{L,\text{tvd}}^n(\hat{\boldsymbol{\xi}}; \boldsymbol{\nu}) \geq 0, \quad n = 1, \dots, N_T \quad (53)$$

using

$$d_{L,\text{tvd}}^n(\hat{\boldsymbol{\xi}}; \boldsymbol{\nu}) \mapsto - \sum_{i=1}^{N-1} \text{sgn}([\mathbf{x}_{\text{ref}}(\boldsymbol{\nu}) + \hat{\boldsymbol{\xi}}_q^n]_{i+1} - [\mathbf{x}_{\text{ref}}(\boldsymbol{\nu}) + \hat{\boldsymbol{\xi}}_q^n]_i) \quad (54)$$

$$([\bar{\boldsymbol{v}}^{n-q}(\mathbf{x}_{\text{ref}}(\boldsymbol{\nu}) + \boldsymbol{\Phi}\hat{\boldsymbol{\xi}}; \boldsymbol{\nu})]_{i+1} - [\bar{\boldsymbol{v}}^{n-q}(\mathbf{x}_{\text{ref}}(\boldsymbol{\nu}) + \boldsymbol{\Phi}\hat{\boldsymbol{\xi}}; \boldsymbol{\nu})]_i)$$

with $d_{L,\text{tvd}}^n : \mathbb{R}^p \times \mathbb{R}^{n_\mu} \rightarrow \mathbb{R}$, $n = 1, \dots, N_T$.

5.3. Constraint on total variation bound (kinematic inequality)

In some cases, schemes enforce a bound on the total variation rather than enforcing a strict total-variation-diminishing constraint due to local degeneracy to first order at critical points. Assuming a given bound b is enforced on the total variation, a total variation bounding constraint (referred to as tvb-constraint in the following)—in the case of the state \boldsymbol{x} corresponding to the value of the solution on a 1D uniformly spaced grid—reads

$$TV(\boldsymbol{x}) \leq b. \quad (55)$$

As a consequence, the Galerkin projection constraint corresponding to optimization problem (31) reads

$$\bar{d}_{G,\text{tvd}}(\hat{\boldsymbol{v}}, \hat{\boldsymbol{\xi}}, \bullet; \boldsymbol{\nu}) \geq 0 \quad \text{if } TV(\mathbf{x}_{\text{ref}}(\boldsymbol{\nu}) + \boldsymbol{\Phi}\hat{\boldsymbol{\xi}}) - b = 0. \quad (56)$$

The LSPG projection constraint corresponding to optimization problem (40) reads

$$\bar{d}_{L,\text{tvb}}^n(\hat{\boldsymbol{\xi}}; \boldsymbol{\nu}) \geq 0, \quad n = 1, \dots, N_T \quad (57)$$

using

$$\bar{d}_{L,\text{tvb}}^n : (\hat{\boldsymbol{\xi}}; \boldsymbol{\nu}) \mapsto b - TV(\mathbf{x}_{\text{ref}}(\boldsymbol{\nu}) + \boldsymbol{\Phi}\hat{\boldsymbol{\xi}}) \quad (58)$$

and $\bar{d}_{L,\text{tvb}}^n : \mathbb{R}^p \times \mathbb{R}^{n_\mu} \rightarrow \mathbb{R}$, $n = 1, \dots, N_T$.

5.4. Constraint on conservation of energy (dynamic equality)

We assume the existence of a history-independent mapping E returning the system energy e from the current state

$$e = E(\boldsymbol{x}) \quad (59)$$

using

$$E : \boldsymbol{\xi} \mapsto E(\boldsymbol{\xi}) \quad (60)$$

with $E : \mathbb{R}^N \rightarrow \mathbb{R}$. Energy conservation (ec) is expressed as the dynamic equality constraint

$$\frac{d}{dt}E(\boldsymbol{x}) = S(t; \boldsymbol{\mu}) \quad (61)$$

or equivalently

$$\frac{\partial E}{\partial \boldsymbol{\xi}}(\boldsymbol{x})^T \dot{\boldsymbol{x}} - S(t; \boldsymbol{\mu}) = 0, \quad (62)$$

wherein we introduced a state-independent source $S : [0, T] \times \mathbb{R}^{n_\mu} \rightarrow \mathbb{R}$ (e.g., a heat source).

The Galerkin projection constraint corresponding to optimization problem (31) reads

$$c_{G,ec}(\hat{\mathbf{v}}, \hat{\boldsymbol{\xi}}, \tau; \boldsymbol{\nu}) = 0 \quad (63)$$

using

$$c_{G,ec} : (\hat{\mathbf{v}}, \hat{\boldsymbol{\xi}}, \tau; \boldsymbol{\nu}) \mapsto \frac{\partial E}{\partial \boldsymbol{\xi}}(\mathbf{x}_{\text{ref}}(\boldsymbol{\nu}) + \boldsymbol{\Phi} \hat{\boldsymbol{\xi}})^T \boldsymbol{\Phi} \hat{\mathbf{v}} - S(\tau; \boldsymbol{\nu}) \quad (64)$$

with $c_{G,ec} : \mathbb{R}^p \times \mathbb{R}^p \times [0, T] \times \mathbb{R}^{n_\mu} \rightarrow \mathbb{R}$.

The LSPG projection constraint corresponding to optimization problem (40) reads

$$c_{L,ec}^n(\hat{\boldsymbol{\xi}}; \boldsymbol{\nu}) = 0, \quad n = 1, \dots, N_T \quad (65)$$

using

$$c_{L,ec}^n : (\hat{\boldsymbol{\xi}}; \boldsymbol{\nu}) \mapsto \frac{\partial E}{\partial \boldsymbol{\xi}}(\mathbf{x}_{\text{ref}}(\boldsymbol{\nu}) + \boldsymbol{\Phi} \hat{\boldsymbol{\xi}}_q^n)^T \bar{\mathbf{v}}^{n-q}(\mathbf{x}_{\text{ref}}(\boldsymbol{\nu}) + \boldsymbol{\Phi} \hat{\boldsymbol{\xi}}; \boldsymbol{\nu}) - S(t^{n-q}; \boldsymbol{\nu}) \quad (66)$$

with $c_{L,ec}^n : \mathbb{R}^p \times \mathbb{R}^{n_\mu} \rightarrow \mathbb{R}$ and $q = 0$ for $\beta_0 \neq 0$ and $q = 1$ for $\beta_0 = 0$ for $n = 1, \dots, N_T$.

6. Numerical experiments

We now present several numerical examples demonstrating the performance and flexibility of the proposed formulation to enforce physical properties across a range of problems. We begin by comparing a constrained and unconstrained projection of FOM solutions onto a low-dimensional subspace. Next, we investigate the performance of the proposed constrained Galerkin and LSPG projection methods for a 1D Burgers' flow problem, a 1D Euler flow problem, and a 2D diffusion problem.

6.1. Error metrics

We employ several error metrics to assess the discrepancy between the time-discrete FOM solution \mathbf{x}^n , $n = 1, \dots, N_T$ and the time-discrete ROM solution $\hat{\mathbf{x}}^n = \mathbf{x}_{\text{ref}}(\boldsymbol{\mu}) + \boldsymbol{\Phi} \hat{\boldsymbol{x}}^n$, $n = 1, \dots, N_T$. In particular, we consider the following metrics:

- the relative state error at time step n :

$$\varepsilon_x^n := \|\mathbf{x}^n - (\mathbf{x}_{\text{ref}}(\boldsymbol{\mu}) + \boldsymbol{\Phi} \hat{\boldsymbol{x}}^n)\|_2 / \|\mathbf{x}^n\|_2, \quad n = 1, \dots, N_T, \quad (67)$$

- the violation of the Galerkin projection rsum-constraint at time step n :

$$\varepsilon_{G,\text{rsum}}^n := \left\| \mathbf{C} \mathbf{r}(\boldsymbol{\Phi} \hat{\boldsymbol{f}}(\hat{\boldsymbol{x}}^n, t^n; \boldsymbol{\mu}), \mathbf{x}_{\text{ref}}(\boldsymbol{\mu}) + \boldsymbol{\Phi} \hat{\boldsymbol{x}}^n, t^n; \boldsymbol{\mu}) \right\|_2, \quad n = 1, \dots, N_T, \quad (68)$$

- the violation of the LSPG projection rsum-constraint at time step n :

$$\varepsilon_{L,\text{rsum}}^n := \|\mathbf{C} \mathbf{r}^n(\mathbf{x}_{\text{ref}}(\boldsymbol{\mu}) + \boldsymbol{\Phi} \hat{\boldsymbol{x}}^n; \boldsymbol{\mu})\|_2, \quad n = 1, \dots, N_T, \quad (69)$$

- the violation of the tvd-constraint at time step n :

$$\varepsilon_{\text{tv}}^n := \max(0, TV(\mathbf{x}_{\text{ref}}(\boldsymbol{\mu}) + \boldsymbol{\Phi} \hat{\boldsymbol{x}}^n) - TV(\mathbf{x}_{\text{ref}}(\boldsymbol{\mu}) + \boldsymbol{\Phi} \hat{\boldsymbol{x}}^{n-1})), \quad n = 1, \dots, N_T, \quad (70)$$

- the violation of the tvb-constraint at time step n :

$$\varepsilon_{\text{tvb}}^n := \max(0, TV(\mathbf{x}_{\text{ref}}(\boldsymbol{\mu}) + \boldsymbol{\Phi} \hat{\boldsymbol{x}}^n) - b), \quad (71)$$

with the upper total variation bound b ,

- the absolute deviation of system energy from the initial condition \mathbf{x}^0 at time step n :

$$\varepsilon_{\text{de}}^n := |E(\mathbf{x}_{\text{ref}}(\boldsymbol{\mu}) + \Phi \hat{\mathbf{x}}^n) - E(\mathbf{x}^0)|, \quad n = 1, \dots, N_T, \quad (72)$$

- the global relative state error:

$$\varepsilon_x := \frac{\sqrt{\sum_{n=1}^{N_T} \|\mathbf{x}^n - (\mathbf{x}_{\text{ref}}(\boldsymbol{\mu}) + \Phi \hat{\mathbf{x}}^n)\|_2^2}}{\sqrt{\sum_{n=1}^{N_T} \|\mathbf{x}^n\|_2^2}} \quad (73)$$

- the mean global violation of the Galerkin projection rsum-constraint:

$$\varepsilon_{G,\text{rsum}} := \frac{1}{N_T} \sqrt{\sum_{n=1}^{N_T} (\varepsilon_{G,\text{rsum}}^n)^2}, \quad (74)$$

- the mean global violation of the LSPG projection rsum-constraint:

$$\varepsilon_{L,\text{rsum}} := \frac{1}{N_T} \sqrt{\sum_{n=1}^{N_T} (\varepsilon_{L,\text{rsum}}^n)^2}, \quad (75)$$

- the mean global violation of the tvd-constraint:

$$\varepsilon_{\text{tv}} := \frac{1}{N_T} \sum_{n=1}^{N_T} \varepsilon_{\text{tv}}^n, \quad (76)$$

- the mean global violation of the tvb-constraint:

$$\varepsilon_{\text{tvb}} := \frac{1}{N_T} \sum_{n=1}^{N_T} \varepsilon_{\text{tvb}}^n, \quad (77)$$

- and the mean global absolute deviation of system energy from the initial condition \mathbf{x}^0 :

$$\varepsilon_{\text{de}} := \frac{1}{N_T} \sum_{n=1}^{N_T} \varepsilon_{\text{de}}^n. \quad (78)$$

6.2. Nonlinear solution strategies

We apply the following solution methods for solving the nonlinear systems and optimization problems that arise at each time step of the considered models.

- FOMs are solved using Newton's method (termination criterion: $\|\mathbf{r}^n(\mathbf{x}^n)\|_2 < 10^{-10}$ or $\|\mathbf{r}^n(\mathbf{x}^n)\|_2 / \|\mathbf{r}^n(\mathbf{x}^{n-1})\|_2 < 10^{-6}$).
- All constrained optimization problems are solved using gradient-based optimization methods with the objective gradient and constraint Jacobians derived analytically and implemented. In this work, we apply the general purpose optimization functionality provided by `scipy.optimize.minimize` (`method='SLSQP'` and `method='trust-constr'`) available in the SciPy [30] (version 1.3.0) scientific computing library of the Python programming language. For problem-specific optimizer settings see Section 6.3 to 6.6.
- The time-discretized Galerkin projection residual (33) is defined implicitly, given that the velocity $\hat{\mathbf{f}}(\boldsymbol{\xi}, \tau; \boldsymbol{\nu})$ is the solution of optimization problem (31). In case of an implicit time stepping scheme, Newton's method would require the evaluation of residual derivatives, including differentiation of the velocity $\hat{\mathbf{f}}(\boldsymbol{\xi}, \tau; \boldsymbol{\nu})$. To avoid this, we apply derivative-free general purpose root finding functionality provided by `scipy.optimize.root` (`method='hybr'` with parameters `maxfev=100`, `xtol=10-6`) available in the SciPy scientific computing library mentioned above to solve the Galerkin OΔE (32) in the case of implicit time integration.

6.3. Kinematics assessment: orthogonal projection vs. constrained projection

In order to demonstrate the potential benefit of kinematic constraints alone, we project the FOM solution onto a low-dimensional subspace using two projection approaches: (1) orthogonal ℓ^2 -projection, and (2) kinematically constrained orthogonal projection using tvb-constraints. The arising optimization problems are solved by `scipy.optimize.minimize` functionality (*method*='trust-constr' with parameters *maxiter*=250, *gtol*= 10^{-6} , *xtol*= 10^{-6} , *barrier_tol*= 10^{-6} , cf. Section 6.2).

Figure 1 shows a solution snapshot $\mathbf{x}^n \in \mathbb{R}^{300}$ (blue curve) of the 1D Euler equations (at the parametric configuration $\boldsymbol{\mu} = (1.6, 1.4)$ and $n = 200$, see Section 6.5 for the problem setup), incorporating the velocity field u , the pressure field p as well as the specific volume field v . Additionally, we plot the orthogonal ℓ^2 -projection of this solution onto the affine subspace $\{\Phi\hat{\mathbf{v}} + \mathbf{x}_{\text{ref}}(\boldsymbol{\mu}) \mid \hat{\mathbf{v}} \in \mathbb{R}^{20}\}$ (red curve) using a reduced-order basis $\Phi \in V_{20}(\mathbb{R}^{300})$ (which is computed from the first 20 POD modes of the FOM solution at parametric configuration $\boldsymbol{\mu} = (1.1, 1.1)$); the resulting solution $\hat{\mathbf{x}}^n \in \mathbb{R}^{20}$ comprises the solution to the optimization problem

$$\underset{\hat{\boldsymbol{\xi}} \in \mathbb{R}^{20}}{\text{minimize}} \quad \left\| \Phi \hat{\boldsymbol{\xi}} + \mathbf{x}_{\text{ref}}(\boldsymbol{\mu}) - \mathbf{x}^n \right\|_2. \quad (79)$$

Remark 6.1. *The orthogonal-projection optimization problem (79) can be equivalently written as $\hat{\mathbf{x}}^n = \Phi^T(\mathbf{x}^n - \mathbf{x}_{\text{ref}}(\boldsymbol{\mu}))$ due to orthogonality of the basis matrix Φ .*

Examination of Figure 1 reveals that the absolute values of the pressure field are several orders of magnitude larger than the velocity field, which in turn exhibits values several orders of magnitude larger than the specific-volume field. As a consequence, the orthogonal ℓ^2 -projection yields an approximation that accurately reproduces the pressure field, but effectively neglects the velocity and specific-volume field.

We observe significant over- and undershoots of the orthogonal projection for velocity and specific volume field. To avoid this, we constrain the projection with a field-specific tvb-constraint of shape (57), choosing the upper bound b as 150% of the total variation of the FOM snapshot, that is, the tvb-constrained projection reads

$$\begin{aligned} & \underset{\hat{\boldsymbol{\xi}} \in \mathbb{R}^{20}}{\text{minimize}} \quad \left\| \Phi \hat{\boldsymbol{\xi}} + \mathbf{x}_{\text{ref}}(\boldsymbol{\mu}) - \mathbf{x}^n \right\|_2 \\ & \text{subject to} \quad \bar{c}_{L,\text{tvb}}^{n,u}(\hat{\boldsymbol{\xi}}; \boldsymbol{\mu}) \geq 0 \\ & \quad \bar{c}_{L,\text{tvb}}^{n,p}(\hat{\boldsymbol{\xi}}; \boldsymbol{\mu}) \geq 0 \\ & \quad \bar{c}_{L,\text{tvb}}^{n,v}(\hat{\boldsymbol{\xi}}; \boldsymbol{\mu}) \geq 0, \end{aligned} \quad (80)$$

wherein we introduced $\bar{c}_{L,\text{tvb}}^{n,u}$, $\bar{c}_{L,\text{tvb}}^{n,p}$ and $\bar{c}_{L,\text{tvb}}^{n,v}$ as the tvb-constraint (57) applied to the individual 1D fields u , p and v .

The reconstruction using tvb-constrained projection is depicted in Figure 1 (green curve). Table 1 depicts relative errors as well as violations of the 150% tvb-constraint obtained by the two investigated projections. We observe an improvement in velocity and specific volume field accuracy at an expense of the pressure field reconstruction accuracy, oscillations in velocity and specific volume field could be reduced.

error	orthogonal projection				constrained projection			
	velocity	pressure	specific volume	total error	velocity	pressure	specific volume	total error
$\varepsilon_{\mathbf{x}}^n$	4.9%	0.073%	12.4%	0.019%	2.7%	6.1%	2.3%	6.1%
$\varepsilon_{\text{tvb}}^n$	73.66	0	0.18	-	0	0	0	-

Table 1: Relative state errors and violation of the tvb-constraint for projection of Euler equations solution snapshot on an affine subspace.

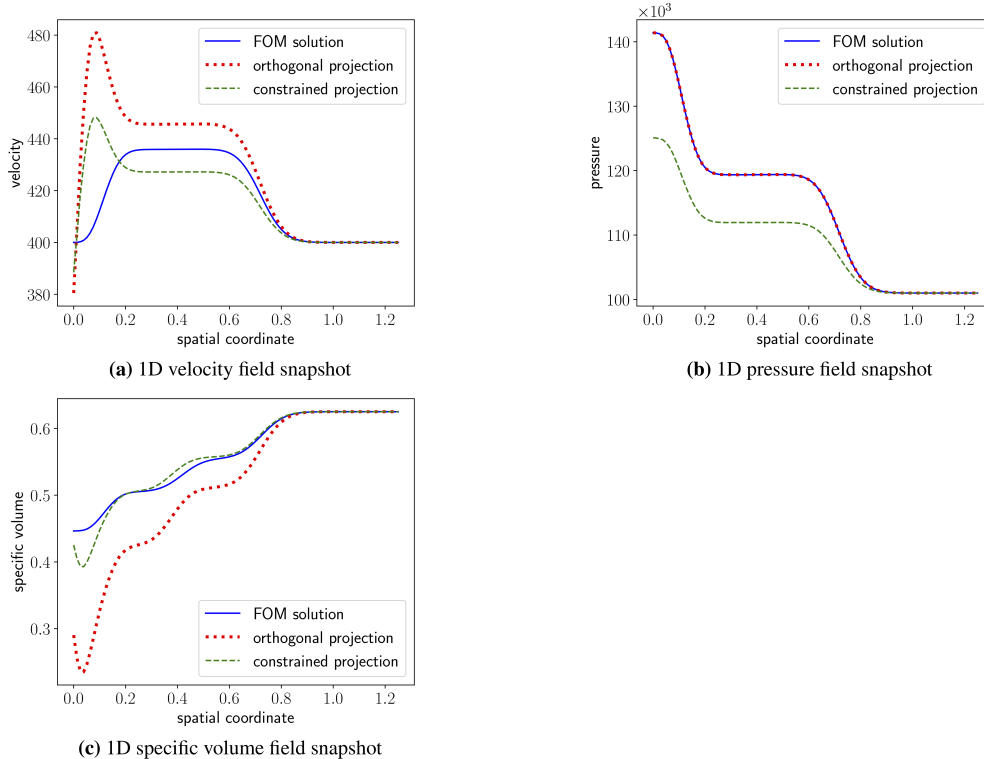


Figure 1: Exemplary FOM solution snapshot of 1D Euler flow, unconstrained orthogonal projection and tvb-constrained projection on the span of a given reduced-order basis.

6.4. Burgers' equation

We demonstrate the performance of the proposed formulation on the source-free and inviscid Burgers' equation

$$\frac{\partial u(z, t; \boldsymbol{\mu})}{\partial t} + u(z, t; \boldsymbol{\mu}) \frac{\partial u(z, t; \boldsymbol{\mu})}{\partial z} = 0, \quad \forall (z, t) \in [0, L] \times [0, T] \quad (81)$$

with the parameterized initial condition

$$u(0, z; \boldsymbol{\mu}) = u_i(z; \boldsymbol{\mu}) \equiv \mu_2 \cos\left(\frac{2\pi\mu_1}{100}z\right) + (\mu_2 + 1), \quad \forall z \in (0, L] \quad (82)$$

and the Dirichlet boundary condition

$$u(0, t; \boldsymbol{\mu}) = u_i(0; \boldsymbol{\mu}), \quad \forall t \in [0, T]. \quad (83)$$

Here, $u(z, t; \boldsymbol{\mu})$ denotes the solution of interest, $z \in [0, L]$ denotes the spatial coordinate (with $L = 100$ being the right boundary), $t \in [0, T]$ denotes time (with $T = 30$ the final time) and $\boldsymbol{\mu} \equiv (\mu_1, \mu_2)$ denote initial-condition parameters corresponding to the frequency and the amplitude (and height), respectively. The parametric domain bounds are given by $\mu_1 \in [0.8; 1.2]$, $\mu_2 \in [0.2; 0.6]$.

6.4.1. Discretization and offline training

We apply a finite-volume scheme with an upwind flux on a uniformly spaced grid, yielding a model with $N = 200$ (i.e., 200 control volumes) degrees of freedom. We apply a backward Euler time discretization with $N_T = 150$ time instances such that $\Delta t = 0.2$. Figure 2 depicts the solution at several time steps for a specific parameter instance.

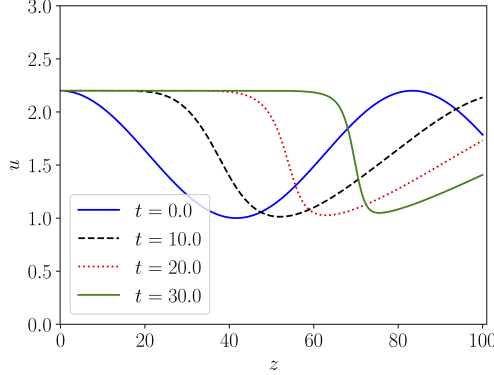


Figure 2: Numerical solution of Burgers' equation at different time steps. The depicted solution corresponds to a parametrization of $\boldsymbol{\mu} = (1.2, 0.6)$.

Training simulations are evaluated on the training set

$$\mathcal{D}_{\text{train}} \equiv \{\boldsymbol{\mu}_{\text{train}}^i\}_{i=1}^{n_{\text{train}}}, \quad \text{with } n_{\text{train}} = 4 \quad (84)$$

resulting from all combination of $\mu_1 \in \{0.8, 1.2\}$ and $\mu_2 \in \{0.2, 0.6\}$. The reduced-order basis $\boldsymbol{\Phi} \in V_p(\mathbb{R}^{200})$ is computed from the first p POD modes of the accumulated snapshot matrix.

6.4.2. Applied constraints

We apply a rsum-constraint of the forms (44) and (46) for constrained Galerkin and LSPG projection, respectively, with a single equality constraint over the sum of all residual entries, that is $\mathbf{C} = [1, 1, \dots, 1]$ with $\mathbf{C} \in \mathbb{R}^{1 \times 200}$. This constraint can be interpreted as global conservation under certain assumptions, see Ref. [8] for a detailed discussion. Furthermore, given that the Burgers' equation under consideration is source-free, the numerical solution of the FOM is total variation diminishing, such that we enforce an inequality constraint of the forms (51) and (53) for constrained Galerkin and LSPG projection, respectively.

6.4.3. Results

All results reported in this section were produced using the functionality of `scipy.optimize.minimize` (`method='SLSQP'` with parameters `maxiter=100`, `ftol=10-10`, cf. Section 6.2). Figures A.5 and A.6 depict error metrics for the Burgers' flow choosing a reduced dimension of $p = 10$. Every model is evaluated at two online parametric configurations, namely $\boldsymbol{\mu}_1 = (0.9, 0.3) \notin \mathcal{D}_{\text{train}}$ and $\boldsymbol{\mu}_2 = (1.3, 0.7) \notin \mathcal{D}_{\text{train}}$. Note that $\boldsymbol{\mu}_1$ and $\boldsymbol{\mu}_2$ correspond to configurations with different complexity in the sense that $\boldsymbol{\mu}_1$ is a setting within the bounds of the training set $\mathcal{D}_{\text{train}}$ while $\boldsymbol{\mu}_2$ resides outside the training set bounds.

The global rsum-constraint, which can be found in subfigures (a) and (b) indicates that with rsum being in use the corresponding error metrics $\varepsilon_{G,\text{rsum}}^n$ and $\varepsilon_{L,\text{rsum}}^n$ decrease locally by several orders of magnitude and achieve near machine precision; this implies that these constraints were feasible.

The violation of the tvd-constraint is depicted in subfigures (c) and (d). Configuration $\boldsymbol{\mu}_1$ fulfills the tvd-constraint for every combination of constraints, even the simple unconstrained ROM is tvd. This changes for configuration $\boldsymbol{\mu}_2$, for which the unconstrained ROM can not maintain diminishing total variation over the entire time of simulation. Turning the tvd-constraint on yields a regain of the desired property, forcing the ROM to inherit the tvd-property from the FOM. This implies that the tvd-constraint was indeed feasible. Subfigures (e) and (f) indicate that the constraints do not have a negative effect on the state error.

Figure A.7 depicts error metrics for $\boldsymbol{\mu}_2$ over a variable reduced-order basis size p . A refinement in p results in decreasing error metrics for the unconstrained models. However, the rsum- as well as the tvd-constraint yield better accuracy in the corresponding error metrics over the entire range, especially for small basis dimensions.

6.5. Euler equations

We now present an ideal gas flow described by the 1D Euler equations

$$\frac{\partial u(z, t; \boldsymbol{\mu})}{\partial t} + u(z, t; \boldsymbol{\mu}) \frac{\partial u(z, t; \boldsymbol{\mu})}{\partial z} + v(z, t; \boldsymbol{\mu}) \frac{\partial p(z, t; \boldsymbol{\mu})}{\partial z} = 0, \quad \forall (z, t) \in [0, L] \times [0, T], \quad (85)$$

$$\frac{\partial p(z, t; \boldsymbol{\mu})}{\partial t} + u(z, t; \boldsymbol{\mu}) \frac{\partial p(z, t; \boldsymbol{\mu})}{\partial z} + \gamma p(z, t; \boldsymbol{\mu}) \frac{\partial u(z, t; \boldsymbol{\mu})}{\partial z} = 0, \quad \forall (z, t) \in [0, L] \times [0, T], \quad (86)$$

$$\frac{\partial v(z, t; \boldsymbol{\mu})}{\partial t} + u(z, t; \boldsymbol{\mu}) \frac{\partial v(z, t; \boldsymbol{\mu})}{\partial z} - v(z, t; \boldsymbol{\mu}) \frac{\partial u(z, t; \boldsymbol{\mu})}{\partial z} = 0, \quad \forall (z, t) \in [0, L] \times [0, T], \quad (87)$$

where the solution is composed of the velocity field $u(z, t; \boldsymbol{\mu})$, the pressure field $p(z, t; \boldsymbol{\mu})$, and the mass-specific volume field $v(z, t; \boldsymbol{\mu})$; here, γ denotes the isentropic exponent. Parametrization in terms of the 2D parameter vector $\boldsymbol{\mu} \equiv (\mu_1, \mu_2)$ is introduced within the initial condition as well as the boundary condition. The initial condition reads

$$u(z, 0; \boldsymbol{\mu}) = u_0, \quad p(z, 0; \boldsymbol{\mu}) = p_0, \quad v(z, 0; \boldsymbol{\mu}) = \frac{1}{\mu_1}, \quad \forall z \in (0, L], \quad (88)$$

and we denote the boundary condition by

$$u(0, t; \boldsymbol{\mu}) = u_{\text{dbc}} = u_0, \quad p(0, t; \boldsymbol{\mu}) = p_{\text{dbc}} = p_0 \mu_2, \quad v(0, t; \boldsymbol{\mu}) = v_{\text{dbc}} = \frac{1}{\mu_1 \mu_2}, \quad \forall t \in [0, T]. \quad (89)$$

The parametrization can be physically interpreted as

$$\mu_1 = \rho_0, \quad \mu_2 = \frac{p_{\text{dbc}}}{p_0} = \frac{\rho_{\text{dbc}}}{\rho_0}. \quad (90)$$

That is, μ_1 corresponds to the initial density of the fluid, while μ_2 corresponds to the ratio of the pressure boundary condition and the initial pressure value and at the same time the ratio of the density boundary condition and the initial density. Consequently, the described setup can be interpreted as a 1D model of a tube, which is continuously traversed by an ideal gas, while at a specific instance in time ($t = 0$), a sudden change in the fluid properties appears at the inlet of the tube.

The constants introduced are set to $\gamma = 1.4$, $u_0 = 400 \frac{\text{m}}{\text{s}}$, $p_0 = 101000 \text{Pa}$, $L = 1.25 \text{m}$ and $T = 0.001 \text{s}$, and the parametric domain bounds are given by $\mu_1 \in [1.1 \frac{\text{kg}}{\text{m}^3}; 1.6 \frac{\text{kg}}{\text{m}^3}]$, $\mu_2 \in [1.1; 1.4]$. Given that the speed of sound is $c = \sqrt{\frac{p_0}{\rho_0} \gamma} < u_0$ (recall that $\rho_0 = \mu_1$), the flow under consideration is classified as supersonic.

6.5.1. Discretization and offline training

We apply a finite-difference spatial discretization scheme on a uniform grid with backward finite differences and $N = 300$ (i.e., 100 degrees of freedom for u, p, v each) and N_T time steps ($N_T = 200$ and $N_T = 600$ will be considered further down below). Time stepping is performed with the explicit Euler method, see Figure 3 for an exemplary solution at several time steps for a specific parameter instance.

Training simulations are evaluated on the training set

$$\mathcal{D}_{\text{train}} \equiv \{\boldsymbol{\mu}_{\text{train}}^i\}_{i=1}^{n_{\text{train}}}, \quad \text{with } n_{\text{train}} = 4 \quad (91)$$

resulting from all combination of $\mu_1 \in \{1.1, 1.6\}$ and $\mu_2 \in \{1.1, 1.4\}$. A reduced-order basis $\boldsymbol{\Phi} \in V_p(\mathbb{R}^{300})$ is computed from the first p POD modes of the training simulation snapshots.

Remark 6.2. *Unconstrained Galerkin and LSPG projection ROMs are equivalent for time discretization by an explicit linear multistep scheme, see Ref. [7]. As a consequence, we depict only one curve for both unconstrained projections in Appendix B.*

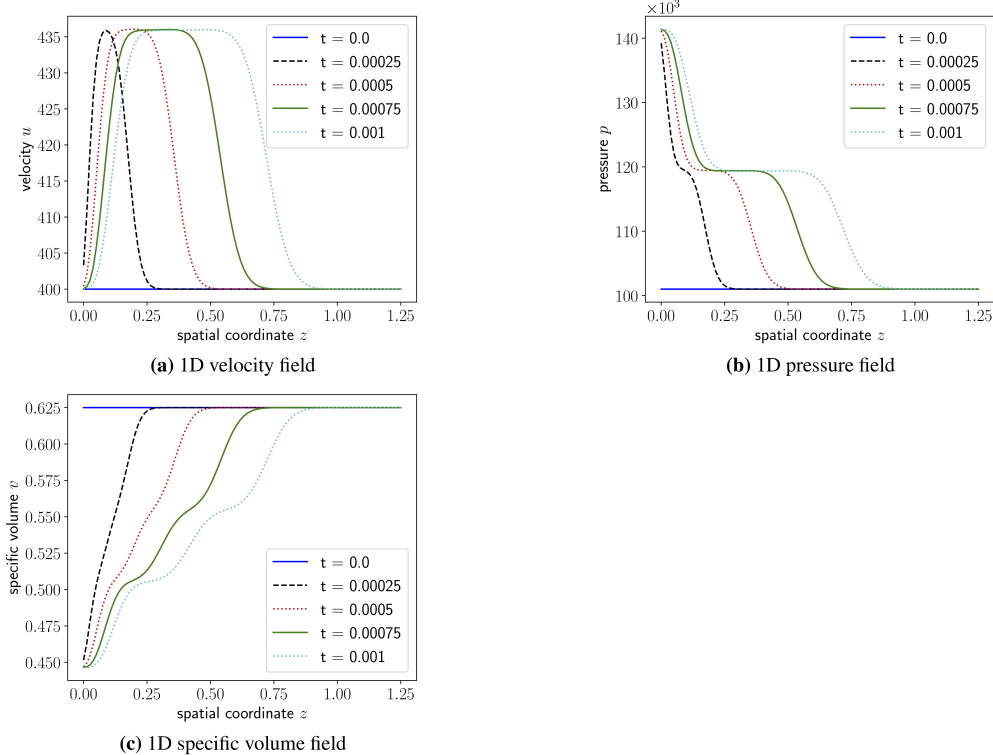


Figure 3: Numerical solution of Euler equations at different time steps. The depicted solution corresponds to a parametrization of $\boldsymbol{\mu} = (1.6, 1.4)$.

6.5.2. Applied constraints

We apply a quantity-specific tvb-constraint of the forms (56) and (57). By quantity-specific we mean that total variation is bounded for each quantity (u , p and v) independently, which results in three inequality constraints. Three total variation bounds (one for each quantity) are computed as 120 % of the quantity-specific maximum total variation values of all training simulation snapshots.

Remark 6.3. *Estimating a total variation bound from training simulation snapshots can be seen as a consistent extension of the snapshot collection method for the construction of a low-dimensional solution subspace, which corresponds to kinematically constraining the space of all admissible solution states. In this context, a total variation bound computed from solution snapshots simply corresponds to further kinematically constraining the state.*

6.5.3. Results

All results reported in this section were produced using the functionality of `scipy.optimize.minimize` (`method='trust-constr'` with parameters `maxiter=250`, `gtol=10-6`, `xtol=10-6`, `barrier.tol=10-6` for Galerkin projection and `method='SLSQP'` with parameters `maxiter=250`, `ftol=10-6` for LSPG projection, cf. Section 6.2). Figures B.8 and B.9 depict results collected from constrained and unconstrained Galerkin and LSPG projections choosing a reduced dimension of $p = 20$. Plots in the left column are computed from 200 time steps, while plots in the right column are computed from a finer discretization in time using 600 time steps. Figure B.8 illustrates relative state errors (67) for the three quantities (velocity $\varepsilon_{x,u}^n$, pressure $\varepsilon_{x,p}^n$, specific volume $\varepsilon_{x,v}^n$) involved in the solution of the Euler equations. The presence of the tvb-constraint improves the state errors. On closer inspection, the plots show an overlap of constrained and unconstrained curves up to a certain point in time, at which the curves split. This observation can be explained by inspecting Figure B.9, which depicts quantity-specific total variations as well as the applied total variation bound. As

a result, the curves in Figure B.8 overlap until the tvb-constraint is active. When the unconstrained curve crosses the total variation bound, state errors start to separate.

Also the total variations in Figure B.9 overlap initially and split, when the tvb-constraint becomes active. However, tvb-constrained curves (especially pronounced for velocity and pressure) still run above the total variation bound for the Galerkin projection, such that the tvb-constraint (55) is not fulfilled. We reference Remark 4.2 for the explanation of this behavior, highlighting that the constraint violation at hand is a consequence of time discretization. Using a finer discretization in time (600 instead of 200 time steps) results in lower constraint violation for the Galerkin projection, which can be seen from right column plots of Figure B.9. For the LSPG projection, the applied total variation bound is strictly respected for 200 as well as 600 time steps.

Figure B.10 depicts mean global error metrics. Discussing the unconstrained ROM first, we observe an initial increase of the state error for all quantities with a peak at $p = 20$, followed by a sudden decrease with increasing reduced-order basis size until $p = 30$. The tvb-constraint violation plots explain the peak at $p = 20$, showing that the unconstrained ROM solution becomes oscillatory. A further increase in p until $p = 30$ leads to a rather accurate ROM, which reflects in the state space error as well as the tvb-constraint violation plots. For further increase in p , the unconstrained ROM again becomes oscillatory at $p = 35$ and eventually unstable at $p = 40$.

In contrast, both tvb-constrained Galerkin and LSPG projection ROMs show only slight (Galerkin projection) or no (LSPG projection) violation of the tvb-constraint over all evaluated reduced-order basis sizes and also achieve a stable solution, when the unconstrained ROM becomes unstable ($p = 40$).

We observe that state errors for some p -values are slightly worse with tvb-constraint activated, while the tvb-constraint is almost fulfilled by the unconstrained curve ($p = 25$ and $p = 30$). The conclusion from the current example is that the tvb-constraint is helpful when the unconstrained ROM severely violates that property, while it can become harmful (for the state error) when the unconstrained ROM is sufficiently accurate by itself.

6.6. Diffusion equation

We solve a nonlinear, non-homogeneous diffusion equation of the shape

$$\rho c \frac{\partial \theta(t, y, z; \boldsymbol{\mu})}{\partial t} - \nabla \cdot (\lambda(\theta) \nabla \theta(t, y, z; \boldsymbol{\mu})) = s(t, y, z; \boldsymbol{\mu}), \quad \forall (t, y, z) \in [0, T] \times [0, L] \times [0, L] \quad (92)$$

with the initial condition

$$\theta(0, y, z; \boldsymbol{\mu}) = 300, \quad \forall (y, z) \in [0, L] \times [0, L], \quad (93)$$

adiabatic boundary conditions

$$\nabla \theta(t, y, z; \boldsymbol{\mu}) \cdot \mathbf{n} = 0, \quad \forall (t, z, y) \in [0, T] \times \{0, L\} \times \{0, L\}, \quad (94)$$

a parameterized source

$$s(t, y, z; \boldsymbol{\mu}) = \underbrace{\mu_1 \delta(y - (0.5 + \mu_4 \sin(2\pi\mu_3 t))) \delta(z - 0.2)}_{s_1} + \underbrace{\mu_2 \delta(y - (0.5 - \mu_4 \sin(2\pi\mu_3 t))) \delta(z - 0.5)}_{s_2}, \quad (95)$$

and a temperature dependent heat conductivity given by

$$\lambda(\theta) = (\theta - 300) + 50. \quad (96)$$

Therein we introduced the area density $\rho = 8000 \text{ kg/m}^2$, mass-specific heat capacity $c = 500 \text{ J/(kg K)}$, temperature θ [K], thermal conductivity λ [W/(m K)], the time $t \in [0, T]$ (with $T = 10000 \text{ s}$ being the end time) and spatial coordinates $(y, z) \in [0, L] \times [0, L]$ (with $L = 1 \text{ m}$ describing the domain size). The parameterized source s consists of two dirac delta δ pulses s_1 and s_2 , which are moving in y -direction in time. Thereby μ_1 [W/m²] and μ_2 [W/m²] are the source strengths, μ_3 [1/s] is the moving frequency and μ_4 [m] the amplitude.

6.6.1. Discretization and offline training

We apply a central finite difference scheme for spatial discretization on a uniform grid yielding $N = 1089$ degrees of freedom (33 in each coordinate axis), and employ the implicit Euler time discretization method with $N_T = 100$ time steps. Figure 4 depicts an exemplary solution at parameter instance $\boldsymbol{\mu} = (-10^6, 10^6, 10^{-4}, 0.2)$ including a source and a sink (negative source strength).

Training simulations are evaluated on the training set

$$\mathcal{D}_{\text{train}} \equiv \{\boldsymbol{\mu}_{\text{train}}^i\}_{i=1}^{n_{\text{train}}}, \quad \text{with } n_{\text{train}} = 8 \quad (97)$$

resulting from all combinations of $(\mu_1, \mu_2) \in \{(-1.1 \times 10^6, 0.9 \times 10^{-6}), (-10^6, 10^{-6})\}$, $\mu_3 \in \{5 \times 10^{-5}, 15 \times 10^{-5}\}$, $\mu_4 \in \{0.1, 0.3\}$ and the reduced-order basis $\boldsymbol{\Phi} \in V_p(\mathbb{R}^{1089})$ is computed from the first p POD modes of the accumulated snapshot matrix.

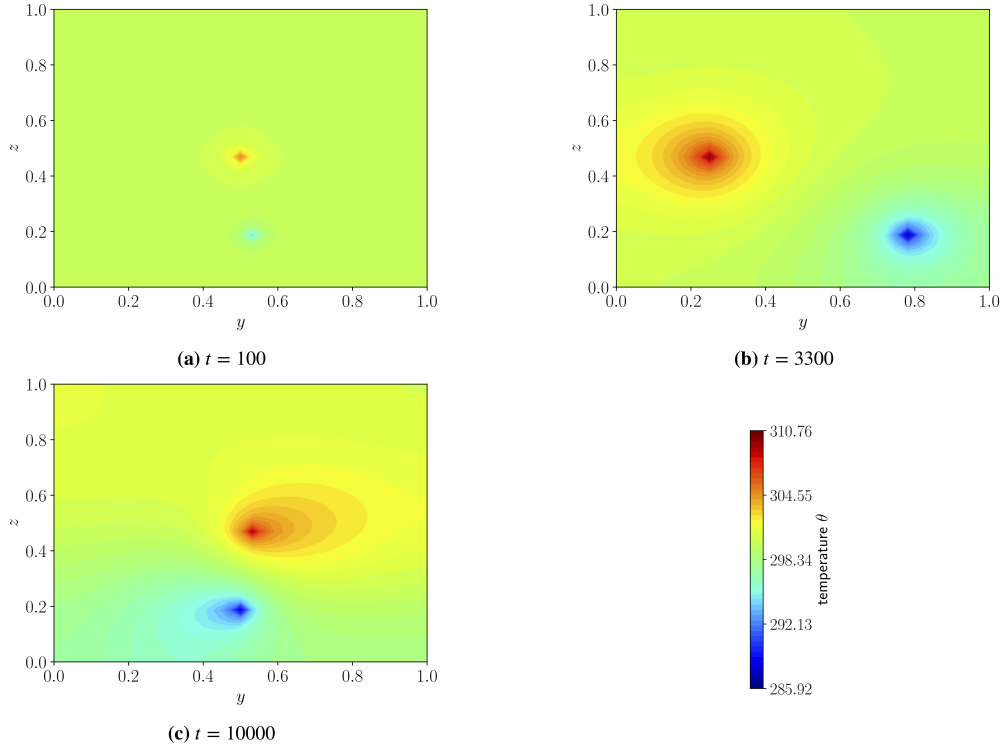


Figure 4: Numerical solution of nonlinear diffusion equation at different time steps. The depicted solution corresponds to a parametrization of $\boldsymbol{\mu} = (-10^6, 10^6, 10^{-4}, 0.2)$.

6.6.2. Applied constraints

We investigate the performance of the proposed reduced-order models for the exemplary parametrization

$$\boldsymbol{\mu} = (-10^6, 10^6, 10^{-4}, 0.2) \quad (98)$$

applying a rsum-constraint of the forms (44) and (46) and an ec-constraint of the forms (63) and (65). The rsum-constraint is set to two equality constraints overlapping in 100 elements, that is

$$\mathbf{C} = \begin{bmatrix} 1 & \dots & \underbrace{1 \dots 1}_{100} & 0 \dots 0 \\ 0 \dots 0 & \underbrace{1 \dots 1}_{100} & \dots & 1 \end{bmatrix} \in \mathbb{R}^{2 \times 1089}. \quad (99)$$

The ec-constraint resolves to a simple form in case of the investigated computational example. The global energy of the computational domain in the continuous setting results from

$$e = \int_0^1 \int_0^1 \rho c \theta(t, y, z; \boldsymbol{\mu}) \, dy dz = \rho c \int_0^1 \int_0^1 \theta(t, y, z; \boldsymbol{\mu}) \, dy dz. \quad (100)$$

Assuming $\boldsymbol{x}(t; \boldsymbol{\mu})$ to be a numerical approximation of the (spatially uniform) discretized temperature field $\theta(t, y, z; \boldsymbol{\mu})$, global energy (100) can be expressed as

$$e = E(\boldsymbol{x}) = \alpha \rho c \mathbf{1}^T \boldsymbol{x}, \quad (101)$$

wherein α is a proportionality constant depending on the spatial discretization (in our case $\alpha = \frac{1}{N} \text{m}^2 = \frac{1}{1089} \text{m}^2$) and $\mathbf{1}$ is a vector of ones. Additionally, source and sink in (98) are of the same absolute strength, which (recalling the adiabatic boundary condition (94)) results in a vanishing energy intake $S(t; \boldsymbol{\mu})$ such that energy conservation (62) can be expressed as

$$\alpha \rho c \mathbf{1}^T \dot{\boldsymbol{x}} = 0 \quad (102)$$

or simply

$$\mathbf{1}^T \dot{\boldsymbol{x}} = 0. \quad (103)$$

6.6.3. Results

All results reported in this section were produced using the functionality of `scipy.optimize.minimize` (`method='SLSQP'` with parameters `maxiter=100`, `ftol=10-10`, cf. Section 6.2). Figure C.11 depicts the violation of the rsum-constraint (68), (69), the deviation of system energy from its initial state (72) and the relative state error (67) for both Galerkin projection and LSPG projection at the parametric configuration (98) and a reduced dimension of $p = 10$. Note that in case of the present example, energy conservation corresponds to a constant system energy, such that energy deviation from the initial state can be interpreted as a violation of conservation of energy. As a result, the rsum-constraint decreases the corresponding error metric by several orders of magnitude to nearly zero, implying feasibility of the rsum-constraint. Similarly, the error in energy conservation drops to nearly zero whenever the ec-constraint is activated, also implying feasibility of this constraint. However, both of these constraints have negligible effect on the state error in this particular case.

Figure C.12 reports global error metrics as a function of ROM dimension p . In all cases, the state error decreases monotonically with increased basis dimension. For any reduced dimension, enforcing the appropriate constraint has a more substantial effect on satisfying the rsum-constraint and ec-constraint than simply increasing the basis dimension. For constrained Galerkin projection, we observe an increased state error for $p = 5$ with rsum- and ec-constraint activated. Obviously the three constraints (two for rsum, one for ec) restrict the five-dimensional solution space in a way that shows a negative impact on the state error. However, we emphasize that this effect vanishes as the ROM dimension increases.

7. Conclusion

This work proposed a novel constrained-optimization formulation model reduction of dynamical systems. In particular, the work proposed both constrained Galerkin and LSPG projection methods that can handle arbitrary kinematic and dynamic constraints of both equality and inequality type. This general framework can be used as a template to enforce particular problem-specific physical properties. This work presented several such examples, including a zero “sum-of-residual-entries” constraint (which can be used to enforce conservation for finite-volume models [8]), a total variation diminishing constraint, a total variation bounding constraint, and an energy-conservation constraint. In three numerical examples, we demonstrated that the proposed framework can indeed be applied in a flexible way to enforce these desired constraints.

Future work will investigate applying the proposed formulation to large-scale dynamical-system models, as well as the realization of computational speedup, which will require including hyper-reduction of the objective

and constraints as needed (as in Ref. [8]), and may also entail developing problem-specific optimizers (e.g., as demonstrated in Refs. [32, 31, 11, 6]). In addition, we will pursue the extension of the proposed method to nonlinear trial manifolds as described in Ref. [18]; this is straightforward, as it amounts to replacing the state and velocity kinematic approximations in equations (6)–(7) with the non-linear trial manifold counterparts

$$\tilde{\mathbf{x}}(t, \boldsymbol{\mu}) := \mathbf{x}_{\text{ref}}(\boldsymbol{\mu}) + \mathbf{g}(\hat{\mathbf{x}}(t, \boldsymbol{\mu})), \quad (104)$$

$$\dot{\tilde{\mathbf{x}}}(t, \boldsymbol{\mu}) = \nabla \mathbf{g}(\hat{\mathbf{x}}(t, \boldsymbol{\mu})) \dot{\hat{\mathbf{x}}}(t, \boldsymbol{\mu}), \quad (105)$$

with $\mathbf{g} : \mathbb{R}^p \rightarrow \mathbb{R}^N$ a continuously differentiable nonlinear operator (e.g., computed via an autoencoder).

The generality of the proposed formulation yields both strengths and weaknesses. Its generality enables it to be used as a template for enforcing a wide variety of physical constraints; however, efficient solvability of the resulting specific ROM formulation remains the responsibility of the end user and may be viewed as a weakness. In our numerical experiments, we identified two situations that can potentially lead to increased state errors if the ROM is constrained. The first situation might occur when the unconstrained ROM is already highly accurate and fulfills the constraints with reasonable accuracy without explicit enforcement. The second situation may occur when the ROM is very low-dimensional (relative to the number of constraints), such that the constraints significantly reduce the number of effective degrees of freedom relative to the unconstrained case. In the case of conservation constraints, we refer the reader to Ref. [8], which performed a detailed study of the effect of different errors on the number of constraints and subspace dimension.

Acknowledgments

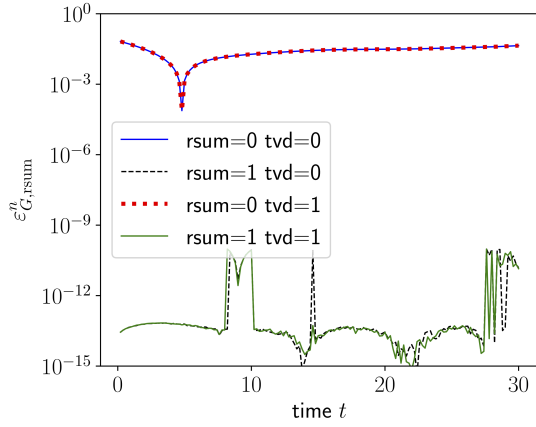
The authors thank Danielle Maddix, Irina Tezaur, Remmelt Ammerlaan, Anran Lu, Yiwen Guo, and Kexin Yu for discussions on this work and related early investigations. This work was sponsored by Sandia’s Advanced Simulation and Computing (ASC) Verification and Validation (V&V) Program and by the Air Force Office of Scientific Research (AFOSR) under award number FA9550-20-1-0236 (MZ). This paper describes objective technical results and analysis. Any subjective views or opinions that might be expressed in the paper do not necessarily represent the views of the U.S. Department of Energy or the United States Government. Sandia National Laboratories is a multimission laboratory managed and operated by National Technology & Engineering Solutions of Sandia, LLC, a wholly owned subsidiary of Honeywell International Inc., for the U.S. Department of Energy’s National Nuclear Security Administration under contract DE-NA0003525.

References

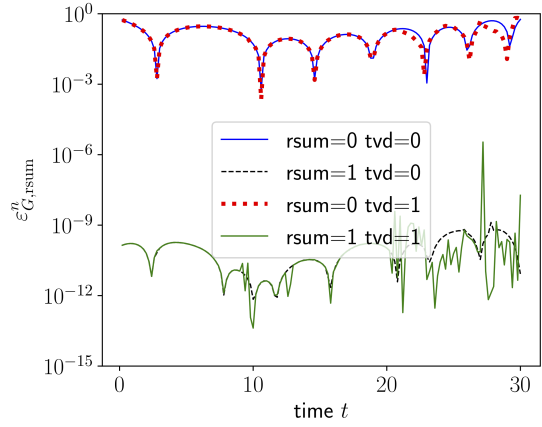
- [1] B. AFKHAM AND J. HESTHAVEN, *Structure preserving model reduction of parametric hamiltonian systems*, SIAM Journal on Scientific Computing, 39 (2017), pp. A2616–A2644.
- [2] B. M. AFKHAM, N. RIPAMONTI, Q. WANG, AND J. S. HESTHAVEN, *Conservative model order reduction for fluid flow*, in Quantification of Uncertainty: Improving Efficiency and Technology, Springer, 2020, pp. 67–99.
- [3] S. AN, T. KIM, AND D. JAMES, *Optimizing cubature for efficient integration of subspace deformations*, ACM Transactions on Graphics (TOG), 27 (2008), p. 165.
- [4] M. BALAJEWICZ, D. AMSALEM, AND C. FARHAT, *Projection-based model reduction for contact problems*, International Journal for Numerical Methods in Engineering, 106 (2016), pp. 644–663.
- [5] M. J. BALAJEWICZ, E. H. DOWELL, AND B. R. NOACK, *Low-dimensional modelling of high-reynolds-number shear flows incorporating constraints from the navier-stokes equation*, Journal of Fluid Mechanics, 729 (2013), p. 285.
- [6] C. CAO, C. NIE, S. PAN, J. CAI, AND K. QU, *A constrained reduced-order method for fast prediction of steady hypersonic flows*, Aerospace Science and Technology, 91 (2019), pp. 679–690.
- [7] K. CARLBERG, M. BARONE, AND H. ANTIL, *Galerkin v. least-squares petrov–galerkin projection in nonlinear model reduction*, Journal of Computational Physics, 330 (2017), pp. 693–734.
- [8] K. CARLBERG, Y. CHOI, AND S. SARGSYAN, *Conservative model reduction for finite-volume models*, Journal of Computational Physics, 371 (2018), pp. 280–314.
- [9] K. CARLBERG, R. TUMINARO, AND P. BOGGS, *Preserving Lagrangian structure in nonlinear model reduction with application to structural dynamics*, SIAM Journal on Scientific Computing, 37 (2015), pp. B153–B184.
- [10] S. CHATURANTABUT AND D. SORENSEN, *Nonlinear model reduction via discrete empirical interpolation*, SIAM Journal on Scientific Computing, 32 (2010), pp. 2737–2764.
- [11] A. CORRIGAN, A. D. KERCHER, AND D. A. KESSLER, *A moving discontinuous galerkin finite element method for flows with interfaces*, International Journal for Numerical Methods in Fluids, 89 (2019), pp. 362–406.
- [12] C. FARHAT, P. AVERY, T. CHAPMAN, AND J. CORTIAL, *Dimensional reduction of nonlinear finite element dynamic models with finite rotations and energy-based mesh sampling and weighting for computational efficiency*, International Journal for Numerical Methods in Engineering, 98 (2014), pp. 625–662.
- [13] C. FARHAT, T. CHAPMAN, AND P. AVERY, *Structure-preserving, stability, and accuracy properties of the energy-conserving sampling and weighting method for the hyper reduction of nonlinear finite element dynamic models*, International Journal for Numerical Methods in Engineering, 102 (2015), pp. 1077–1110.
- [14] L. FICK, Y. MADAY, A. PATERA, AND T. TADDEI, *A stabilized pod model for turbulent flows over a range of reynolds numbers: Optimal parameter sampling and constrained projection*, Journal of Computational Physics, 371 (2018), pp. 214–243.
- [15] C. HUANG, K. DURAISAMY, AND C. L. MERKLE, *Investigations and improvement of robustness of reduced-order models of reacting flow*, AIAA Journal, 57 (2019), pp. 5377–5389.
- [16] S. LALL, P. KRYSL, AND J. MARSDEN, *Structure-preserving model reduction for mechanical systems*, Physica D: Nonlinear Phenomena, 184 (2003), pp. 304–318.

- [17] K. LEE AND K. CARLBERG, *Deep conservation: A latent dynamics model for exact satisfaction of physical conservation laws*, arXiv preprint arXiv:1909.09754, (2019).
- [18] K. LEE AND K. T. CARLBERG, *Model reduction of dynamical systems on nonlinear manifolds using deep convolutional autoencoders*, Journal of Computational Physics, 404 (2020), p. 108973.
- [19] C. LEHRENFELD AND S. RAVE, *Mass conservative reduced order modeling of a free boundary osmotic cell swelling problem*, Advances in Computational Mathematics, (2019).
- [20] J.-C. LOISEAU AND S. BRUNTON, *Constrained sparse galerkin regression*, Journal of Fluid Mechanics, 838 (2018), pp. 42–67.
- [21] M. MOHEBUJJAMAN, L. G. REBHOLZ, AND T. ILIESCU, *Physically constrained data-driven correction for reduced-order modeling of fluid flows*, International Journal for Numerical Methods in Fluids, 89 (2019), pp. 103–122.
- [22] M. MOHEBUJJAMAN, L. G. REBHOLZ, X. XIE, AND T. ILIESCU, *Energy balance and mass conservation in reduced order models of fluid flows*, Journal of Computational Physics, 346 (2017), pp. 262–277.
- [23] L. PENG AND K. MOHSENI, *Symplectic model reduction of hamiltonian systems*, SIAM Journal on Scientific Computing, 38 (2016), pp. A1–A27.
- [24] R. POLYUGA AND A. VAN DER SCHAFT, *Structure preserving model reduction of port-hamiltonian systems by moment matching at infinity*, Automatica, 46 (2010), pp. 665–672.
- [25] A. QUARTERONI, G. ROZZA, AND A. MANZONI, *Certified reduced basis approximation for parametrized partial differential equations and applications*, Journal of Mathematics in Industry, 1 (2011), pp. 1–49.
- [26] M. RATHINAM AND L. PETZOLD, *A new look at proper orthogonal decomposition*, SIAM Journal on Numerical Analysis, 41 (2003), pp. 1893–1925.
- [27] S. REDDY, B. FRENO, P. CIZMAS, S. GOKALTUN, D. MCDANIEL, AND G. DULIKRAVICH, *Constrained reduced-order models based on proper orthogonal decomposition*, Computer Methods in Applied Mechanics and Engineering, 321 (2017), pp. 18–34.
- [28] C. W. ROWLEY, T. COLONIUS, AND R. M. MURRAY, *Model reduction for compressible flows using pod and galerkin projection*, Physica D: Nonlinear Phenomena, 189 (2004), pp. 115–129.
- [29] B. SANDERSE, *Non-linearly stable reduced-order models for incompressible flow with energy-conserving finite volume methods*, Journal of Computational Physics, 421 (2020), p. 109736.
- [30] P. VIRTANEN, R. GOMMERS, T. E. OLIPHANT, ET AL., *Scipy 1.0: Fundamental algorithms for scientific computing in python*, Nature Methods, 17 (2020), pp. 261–272.
- [31] M. J. ZAHR, A. SHI, AND P.-O. PERSSON, *Implicit shock tracking using an optimization-based high-order discontinuous galerkin method*, Journal of Computational Physics, 410 (2020), p. 109385.
- [32] R. ZIMMERMANN, A. VENDL, AND S. GÖRTZ, *Reduced-order modeling of steady flows subject to aerodynamic constraints*, AIAA journal, 52 (2014), pp. 255–266.

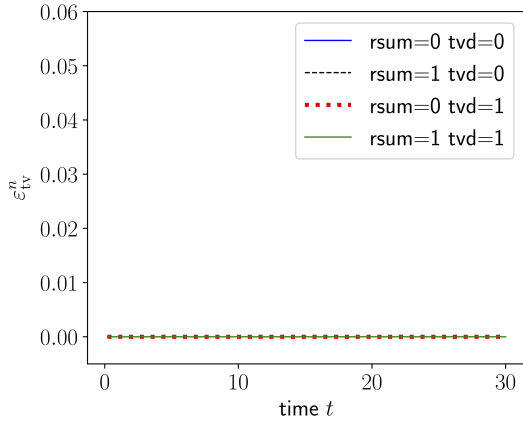
Appendix A. Burgers' equation



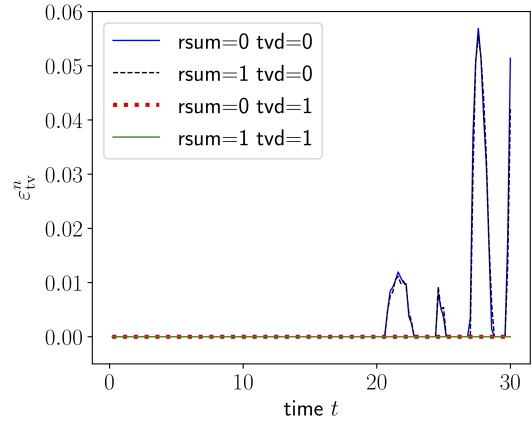
(a) rsum-constraint at μ_1



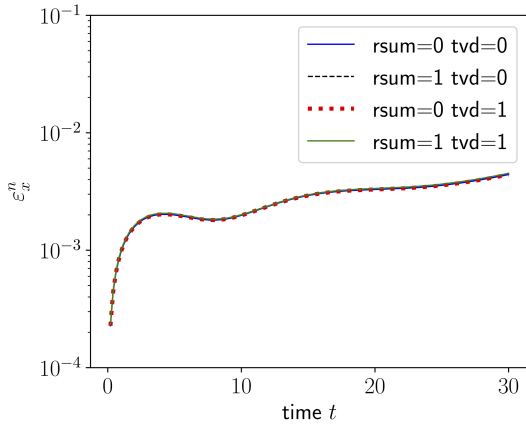
(b) rsum-constraint at μ_2



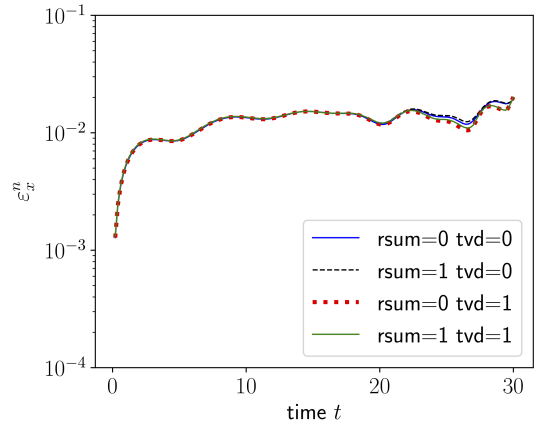
(c) Violation of tvd-property at μ_1



(d) Violation of tvd-property at μ_2

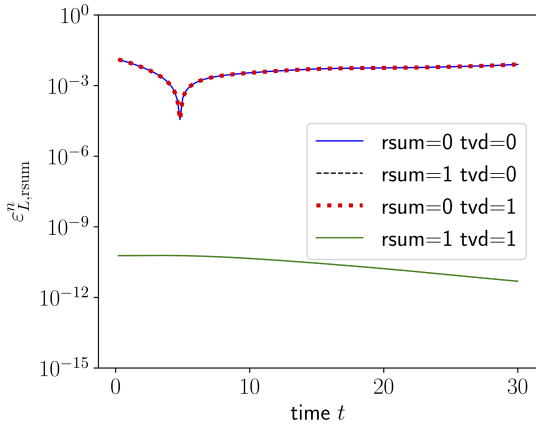


(e) Relative state error at μ_1

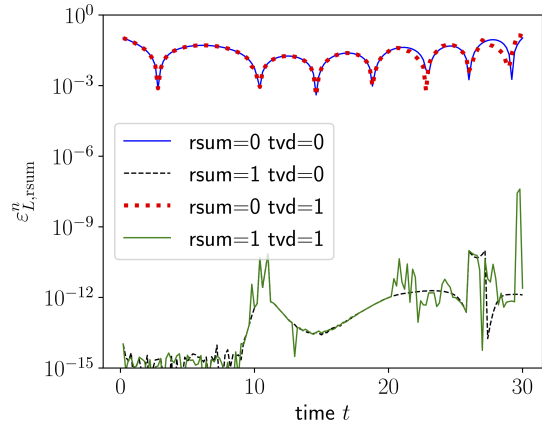


(f) Relative state error at μ_2

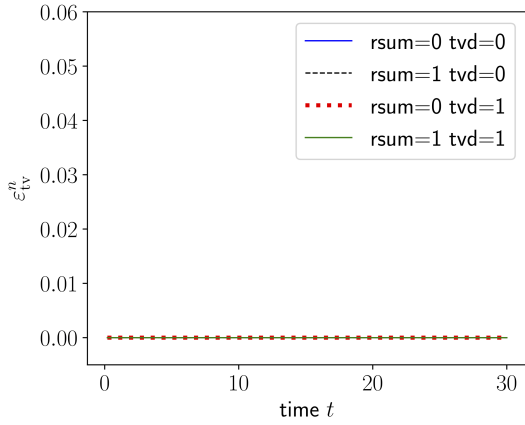
Figure A.5: 1D Burgers' equation. Error metrics for the Galerkin projection (10 degrees of freedom) evaluated at $\mu_1 = (0.9, 0.3)$ and $\mu_2 = (1.3, 0.7)$. rsum = 0/1 and tvd = 0/1 denote the sum-of-residual-entries constraint and total variation diminishing constraint being *not in use* / *in use*.



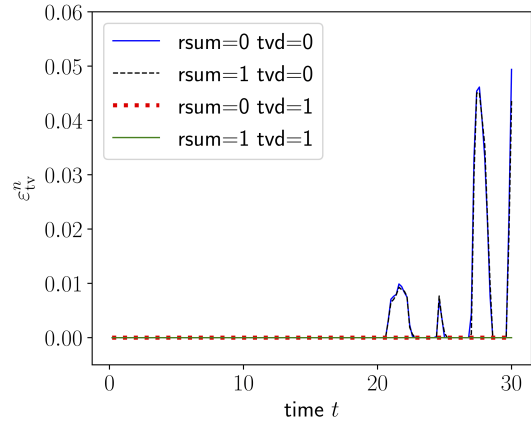
(a) rsum-constraint at μ_1



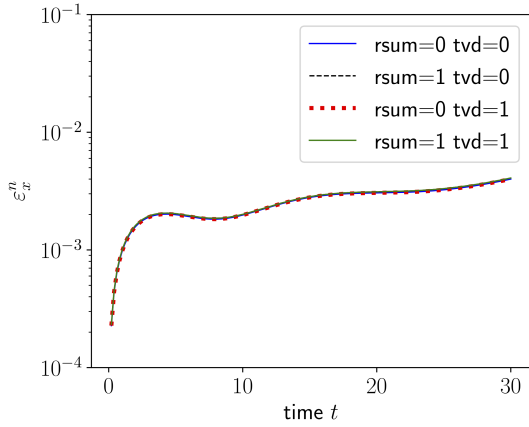
(b) rsum-constraint μ_2



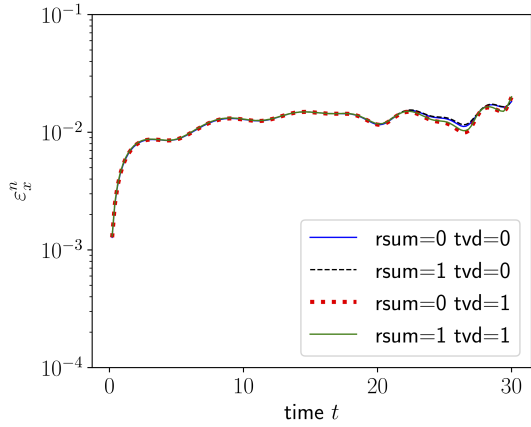
(c) Violation of tvd-property at μ_1



(d) Violation of tvd-property at μ_2

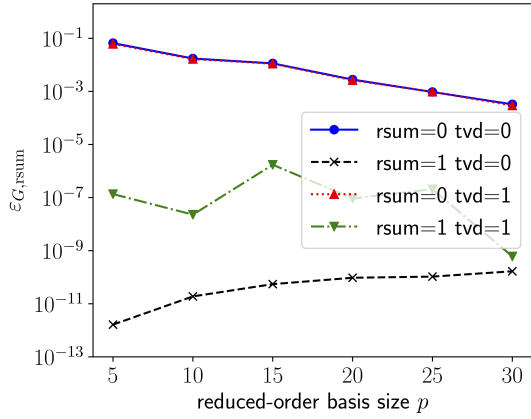


(e) Relative state error at μ_1

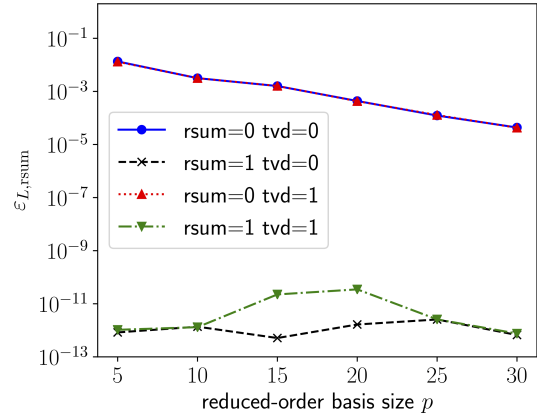


(f) Relative state error at μ_2

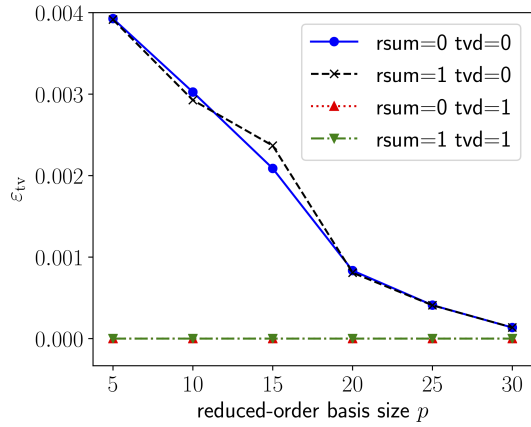
Figure A.6: 1D Burgers' equation. Error metrics for the LSPG projection (10 degrees of freedom) evaluated at $\mu_1 = (0.9, 0.3)$ and $\mu_2 = (1.3, 0.7)$. rsum = 0/1 and tvd = 0/1 denote the sum-of-residual-entries constraint and total variation diminishing constraint being *not in use* / *in use*.



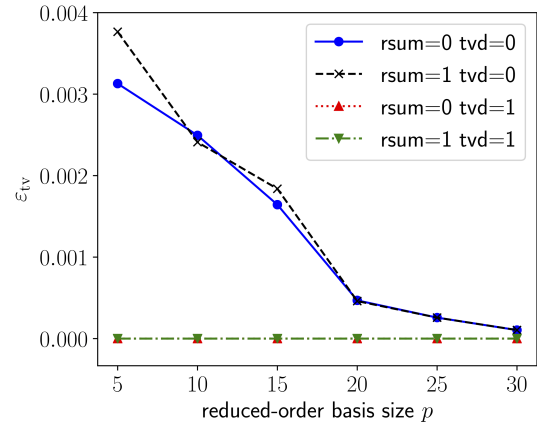
(a) Mean global Galerkin projection rsum-constraint



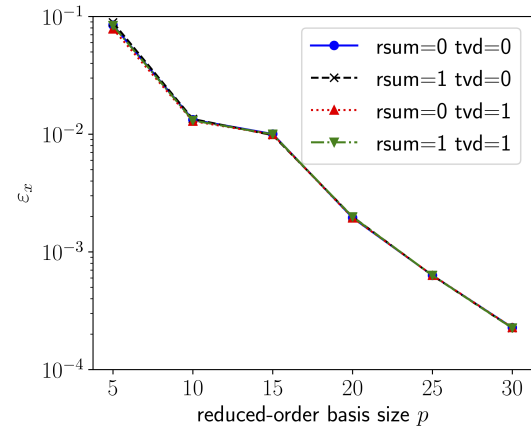
(b) Mean global LSPG projection rsum-constraint



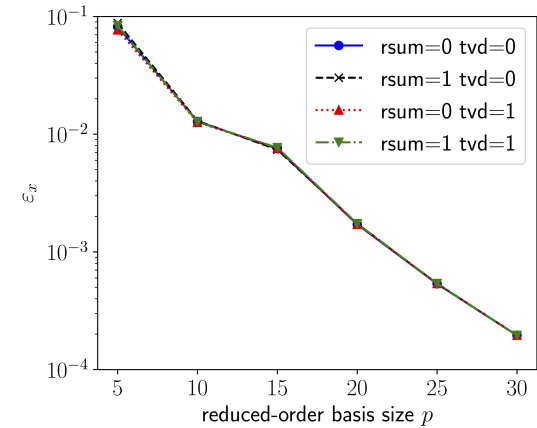
(c) Mean global Galerkin projection violation of tvd-property



(d) Mean global LSPG projection violation of tvd-property



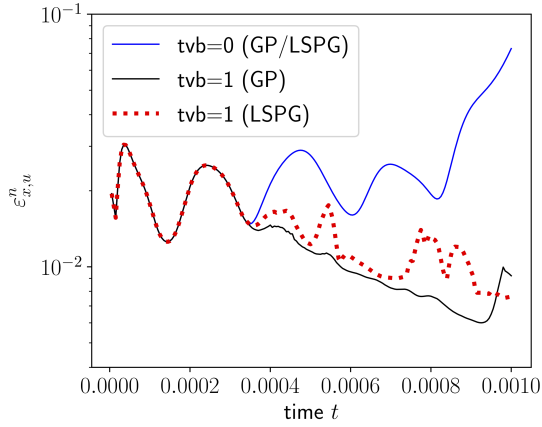
(e) Global relative Galerkin projection state error



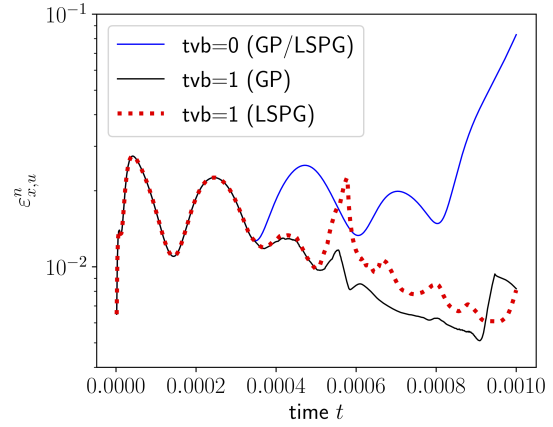
(f) Global relative LSPG projection state error

Figure A.7: 1D Burgers' equation. Galerkin projection (left column) and LSPG projection (right column) global error metrics over variable reduced-order basis size evaluated at $\mu_2 = (1.3, 0.7)$. rsum = 0/1 and tvd = 0/1 denote the sum-of-residual-entries constraint and total variation diminishing constraint being *not in use* / *in use*.

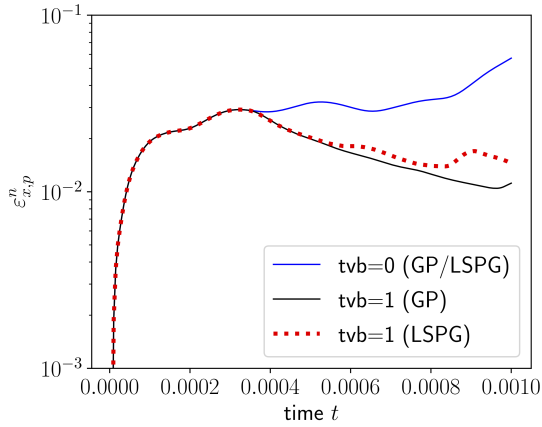
Appendix B. Euler equations



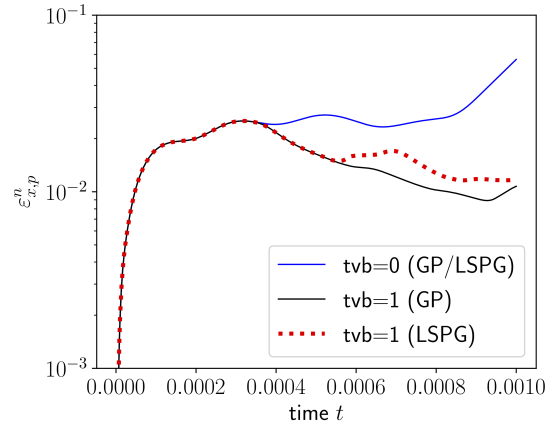
(a) Velocity relative state error ($N_T = 200$)



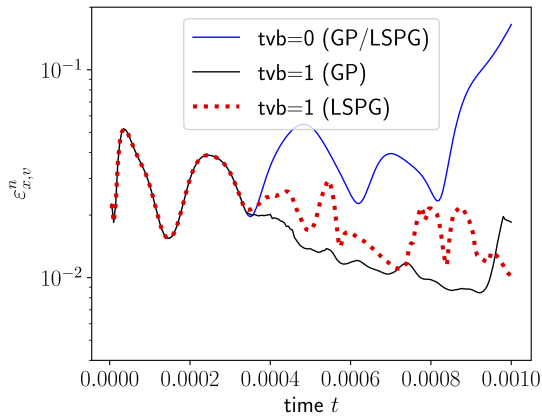
(b) Velocity relative state error ($N_T = 600$)



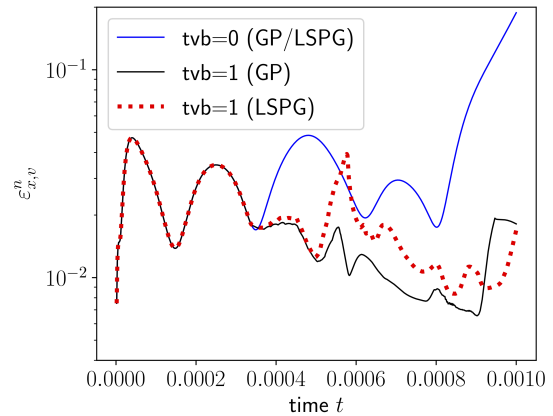
(c) Pressure relative state error ($N_T = 200$)



(d) Pressure relative state error ($N_T = 600$)

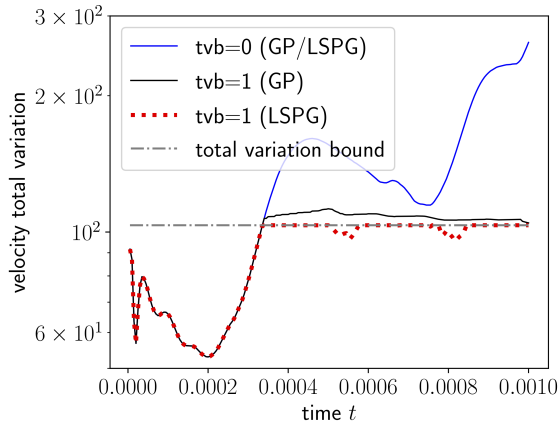


(e) Specific volume relative state error ($N_T = 200$)

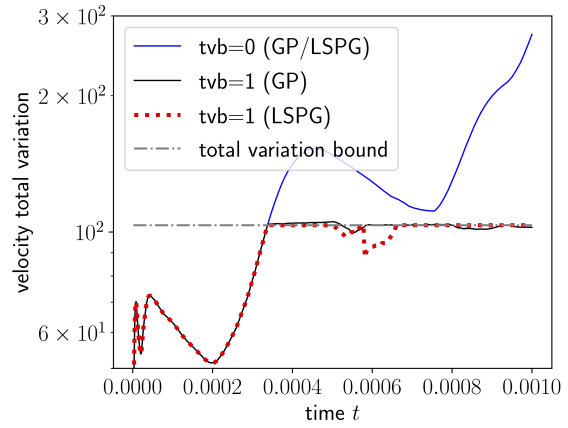


(f) Specific volume relative state error ($N_T = 600$)

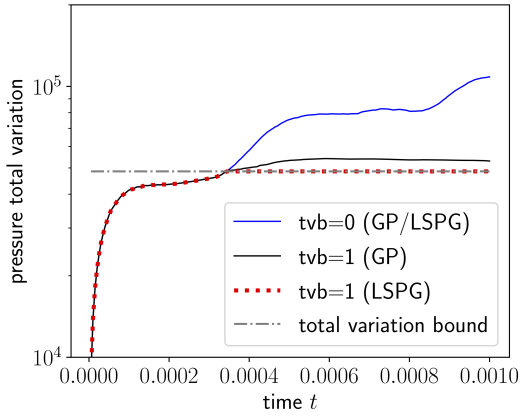
Figure B.8: 1D Euler equations. State errors for Galerkin projection (20 degrees of freedom) evaluated at $\mu = (1.25, 1.5)$. Left column plots were produced with 200 time steps and right column plots with 600 time steps. $\text{tvb} = 0/1$ denotes the total variation bounding constraint being *not in use* / *in use*. Unconstrained GP and LSPG are equivalent due to explicit discretization in time.



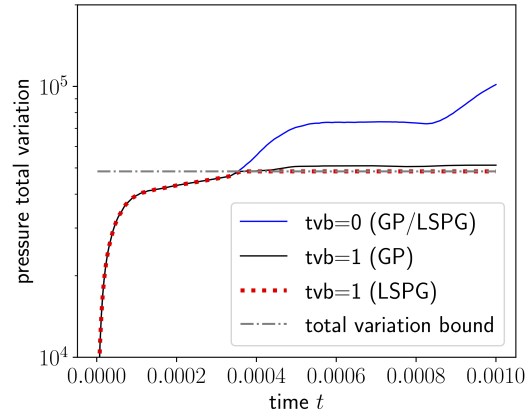
(a) Velocity relative state error ($N_T = 200$)



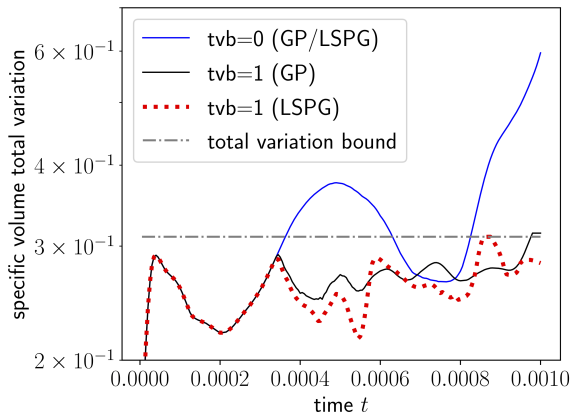
(b) Velocity relative state error ($N_T = 600$)



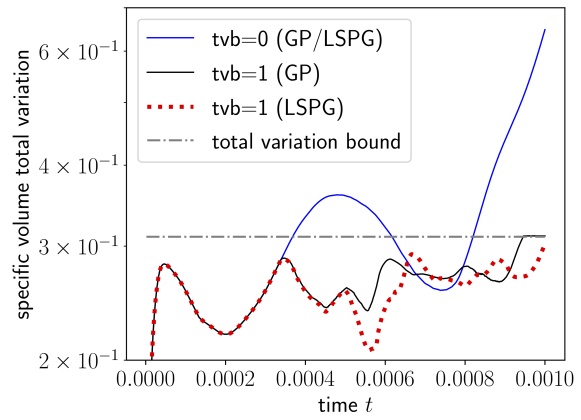
(c) Pressure relative state error ($N_T = 200$)



(d) Pressure relative state error ($N_T = 600$)

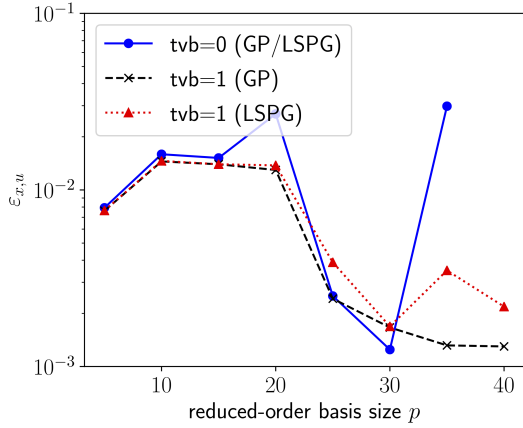


(e) Specific volume relative state error ($N_T = 200$)

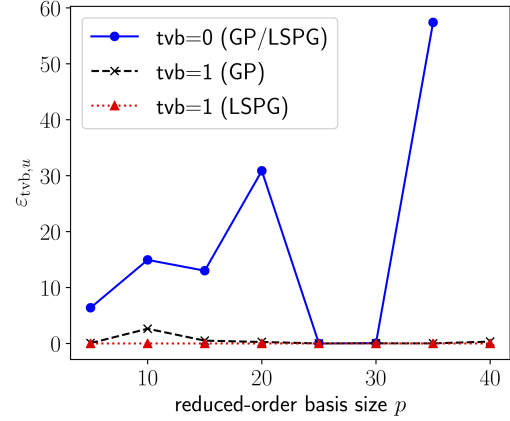


(f) Specific volume relative state error ($N_T = 600$)

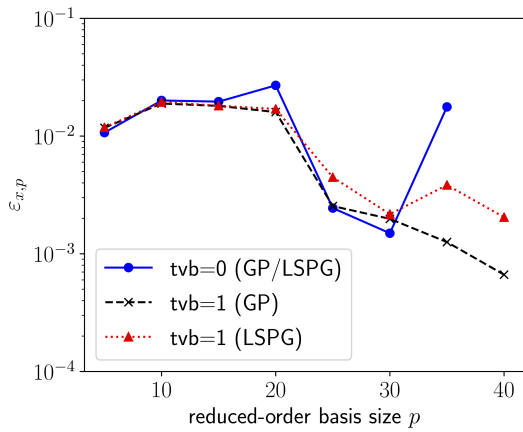
Figure B.9: 1D Euler equations. State total variations for Galerkin projection (GP) and LSPG projection (LSPG) (20 degrees of freedom) evaluated at $\mu = (1.25, 1.5)$. Left column plots were produced with 200 time steps and right column plots with 600 time steps. $\text{tvb} = 0/1$ denotes the total variation bounding constraint being *not in use* / *in use*. Unconstrained GP and LSPG are equivalent due to explicit discretization in time.



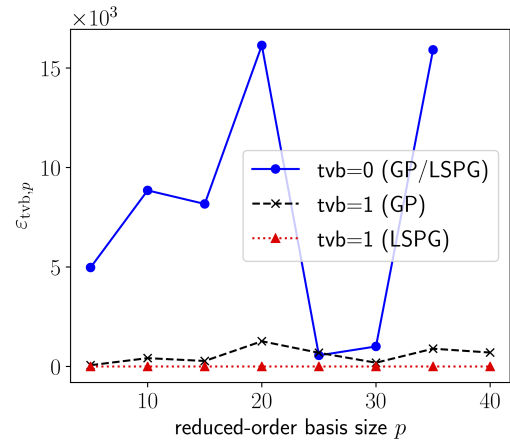
(a) Global velocity relative state error



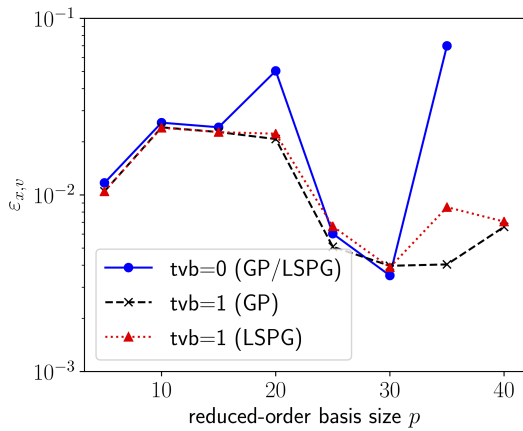
(b) Mean global velocity tvb-constraint violation



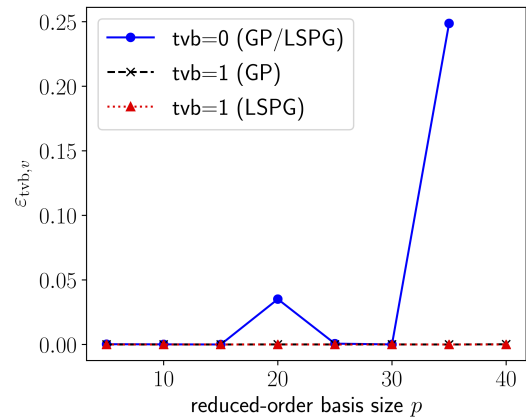
(c) Global pressure relative state error



(d) Mean global pressure tvb-constraint violation



(e) Global specific volume relative state error



(f) Mean global specific volume tvb-constraint violation

Figure B.10: 1D Euler equations. Galerkin projection (GP) and LSPG projection (LSPG) global state errors (left column) and mean global total variation bounding constraint violation (right column) at 600 time steps. $tvb = 0/1$ denotes the total variation bounding constraint being *not in use* / *in use*. The unconstrained projection ROM ($tvb=0$) was unstable for $p = 40$. Unconstrained GP and LSPG are equivalent due to explicit discretization in time.

Appendix C. Diffusion equation

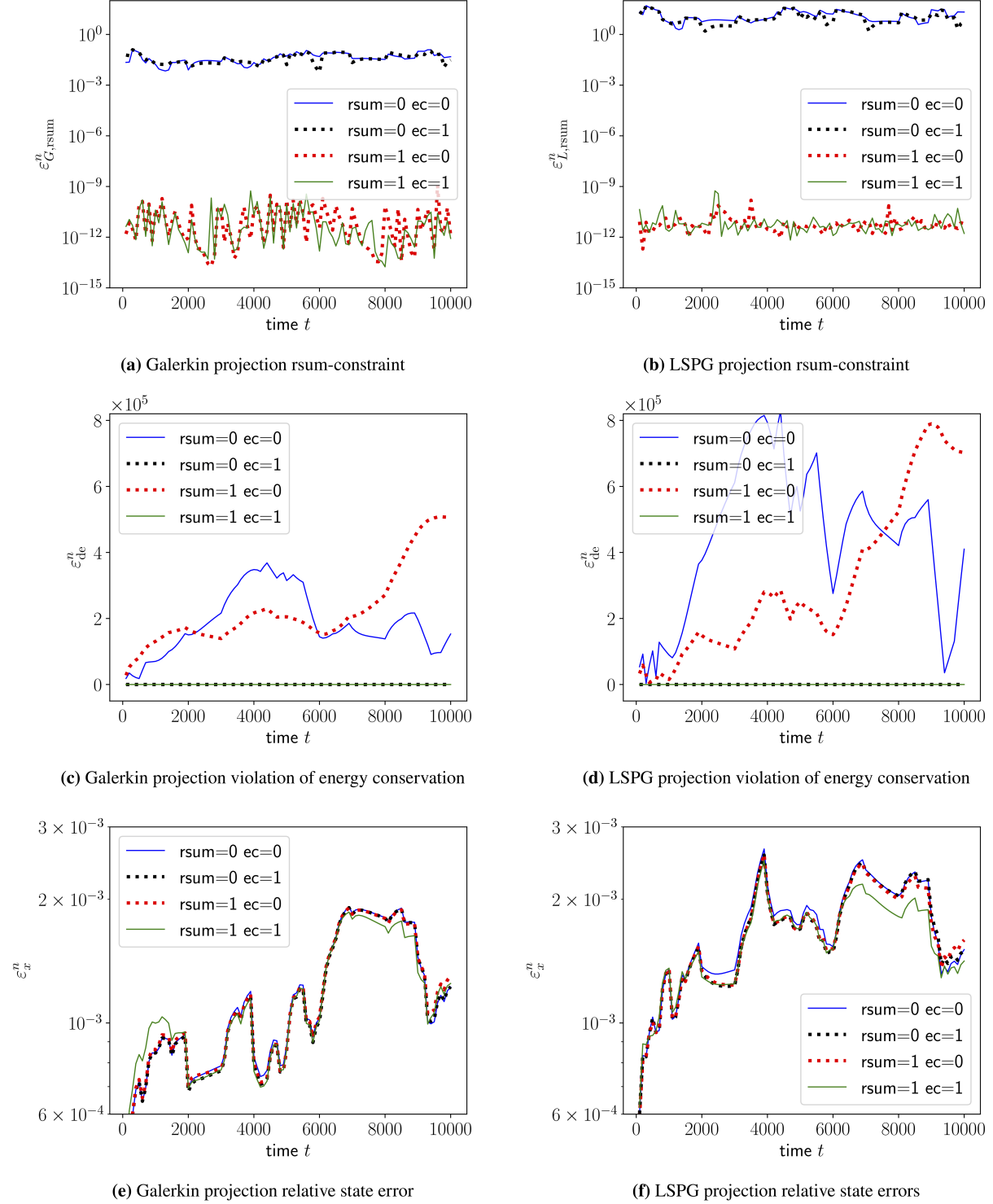
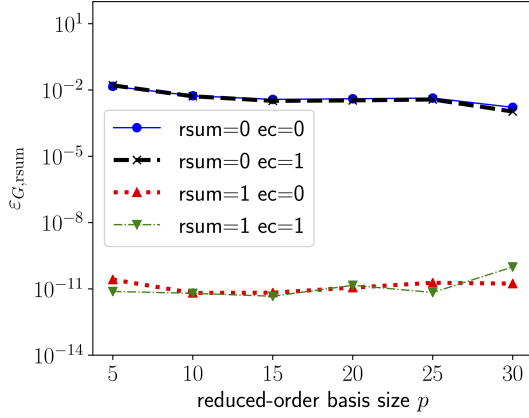
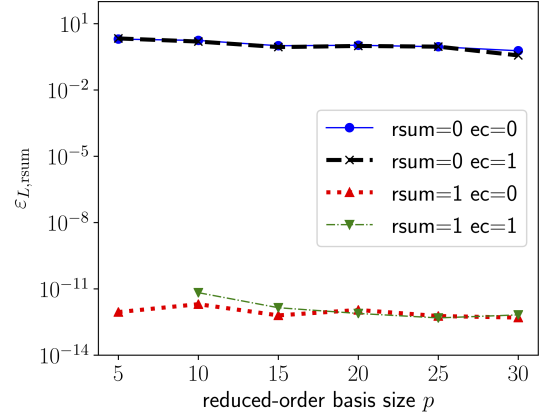


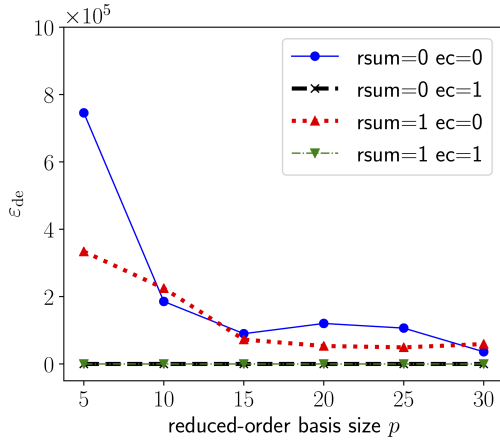
Figure C.11: 2D diffusion problem. Error metrics for the Galerkin projection (left column plots) and LSPG projection (right column plots) (10 degrees of freedom) evaluated at $\mu = (10^6, -10^6, 10^{-4}, 0.2)$ with 100 time steps. rsum = 0/1 and ec = 0/1 denote the sum-of-residual-entries constraint and energy conservation constraint being *not in use* / *in use*.



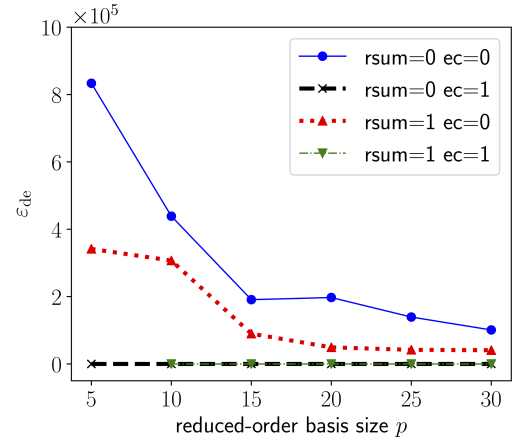
(a) Mean global Galerkin projection rsum-constraint



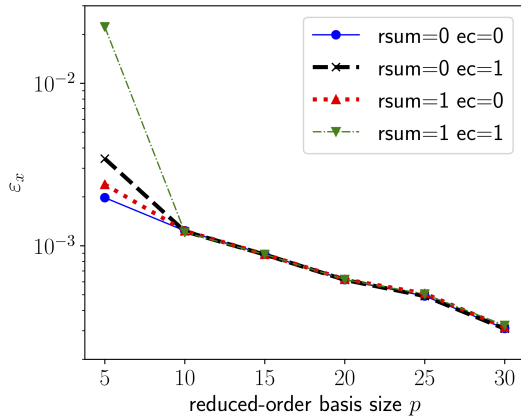
(b) Mean global LSPG projection rsum-constraint



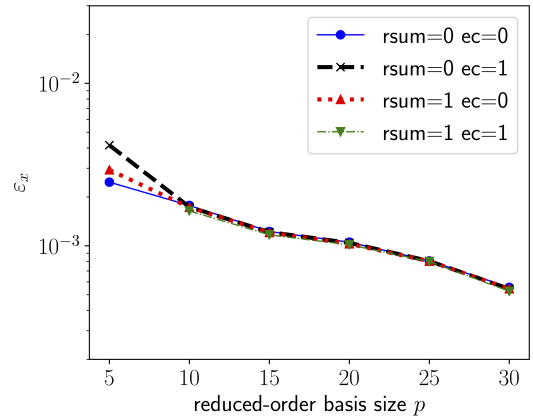
(c) Mean global Galerkin projection violation of ec



(d) Mean global LSPG projection violation of ec



(e) Global Galerkin projection relative state error



(f) Global LSPG projection relative state error

Figure C.12: 2D diffusion problem. Galerkin projection (left column) and LSPG projection (right column) global error metrics over variable basis size evaluated at $\mu = (10^6, -10^6, 10^{-4}, 0.2)$ with 100 time steps. $rsum = 0/1$ and $ec = 0/1$ denote the sum-of-residual-entries constraint and energy conservation constraint being *not in use* / *in use*. The simulation $rsum=1, ec=1$, $p = 5$ in case of the LSPG projection failed to converge and is therefore not depicted.

Appendix D. Problem-specific constraints

nomenclature	interpretation	constraint	reference
$\boldsymbol{\theta}$: discretized temperature field θ_l : lower temperature bound θ_u : upper temperature bound	bounded temperature to physical range	$\min(\boldsymbol{\theta}) - \theta_l \geq 0$ $\theta_u - \max(\boldsymbol{\theta}) \geq 0$	Ref. [15]
$\bar{\mathbf{C}}$: subdomain conservation matrix \mathbf{r} : time-continuous residual \mathbf{r}^n : time-discrete residual	conservation in finite-volume models	$\bar{\mathbf{C}}\mathbf{r} = \mathbf{0}$ $\bar{\mathbf{C}}\mathbf{r}^n = \mathbf{0}$	Ref. [8]
$C_{L,(\text{target})}$: (target) lift coefficient $C_{D,(\text{target})}$: (target) drag coefficient	fulfillment of aerodynamic constraints	$C_L - C_{L,\text{target}} = 0$ $C_D - C_{D,\text{target}} = 0$	Ref. [32]
$\boldsymbol{\lambda}$:Lagrange multipliers (in solid mechanics contact problem)	positivity of contact forces in solid mechanics contact problem	$\boldsymbol{\lambda} \geq \mathbf{0}$	Ref. [4]
K : kinetic energy \mathbf{u} : velocity field ν : kinematic viscosity	kinetic energy balance in incompressible flows (under given modeling assumptions, see Ref. [29])	$\frac{dK}{dt} + \nu \ \nabla \mathbf{u}\ ^2 = 0$	Ref. [29]
$\hat{\mathbf{x}}_l$: lower bounds on generalized coordinates $\hat{\mathbf{x}}_u$: upper bounds on generalized coordinates	bounded ROM solution by hyper-parameters estimated from FOM	$\hat{\mathbf{x}} - \hat{\mathbf{x}}_l \geq \mathbf{0}$ $\hat{\mathbf{x}}_u - \hat{\mathbf{x}} \geq \mathbf{0}$	Ref. [14]

Table D.2: Examples for constraints (with references) representable by the general constraint set (16) - (19). Note, that the constraint on bounded generalized coordinates (last row) is not directly representable by our general constraint set, which is defined independently from the ROM solution. We nevertheless include the constraint on bounded generalized coordinates, recalling that the generalized coordinates are expressible in terms of the FOM state $\hat{\mathbf{x}} = \boldsymbol{\Phi}^T(\mathbf{x} - \mathbf{x}_{\text{ref}}(\boldsymbol{\mu}))$.